Deep Learning of Multiresolution X-Ray Micro-Computed-Tomography Images for Multiscale Modeling

Samuel J. Jackson,[1,*] Yufu Niu,[2] Sojwal Manoorkar,[3] Peyman Mostaghimi,[2] and Ryan T. Armstrong[2]

[1] *CSIRO Energy, Private Bag 10, Clayton South, Victoria 3169, Australia*

[2] *School of Minerals and Energy Resources Engineering, University of New South Wales, Sydney, New South Wales 2052, Australia*

[3] *Department of Earth Science and Engineering, Imperial College London, London SW7 2BP, United Kingdom*

(Received 2 November 2021; revised 15 March 2022; accepted 18 March 2022; published 27 May 2022)

Field-of-view and resolution trade-offs in x-ray micro-computed-tomography (micro-CT) imaging limit the characterization, analysis, and model development of multiscale porous systems. To this end, we develop an applied methodology utilizing deep learning to enhance low-resolution (LR) images over large sample sizes and create multiscale models capable of accurately simulating experimental fluid dynamics from the pore (microns) to continuum (centimeters) scale. We develop a three-dimensional (3D) enhanced deep-superresolution (EDSR) convolutional neural network to create superresolution (SR) images from LR images, which alleviates common micro-CT hardware and/or reconstruction defects in high-resolution (HR) images. When paired with pore-network simulations and parallel computation, we can create large 3D continuum-scale models with spatially varying flow and material properties. We quantitatively validate the workflow at various scales using direct HR and SR image similarity, pore-scale material and/or flow simulations, and continuum-scale multiphase-flow experiments (drainage-immiscible flow pressures and 3D fluid-volume fractions). The SR images and models are comparable to the HR ground truth and generally accurate to within experimental uncertainty at the continuum scale across a range of flow rates. They are found to be significantly more accurate than their LR counterparts, especially in cases where a wide distribution of pore sizes are encountered. The applied methodology opens up the possibility to image, model, and analyze truly multiscale heterogeneous systems that are otherwise intractable.

DOI: 10.1103/PhysRevApplied.17.054046

I. INTRODUCTION

Multiphase porous materials are ubiquitous in engineered and natural systems, e.g., in electrochemical applications such as fuel cells or batteries [1], in organic matter such as blood vessels [2], and in geological media such as sandstone or carbonate rocks [3]. In these systems, heterogeneities in the porous structure often exist at multiple scales, which can range from micrometers to kilometers in the case of the geological subsurface [4]. The smaller-scale heterogeneities can often have larger-scale macroscopic impacts [5] and understanding the interaction between multiscale heterogeneities is key to predicting large-scale phenomena [6]. However, methodologies to characterize and model multiscale heterogeneous systems in a tractable way are lacking. From a materials-science point of view, multiscale heterogeneities are increasingly being used to optimize function, in bio(inspired) materials, structural materials, and heterogeneous catalysts [7]. Therefore, an applied approach to model flow in multiscale heterogeneous systems is needed for advancements in the material sciences and geology-based disciplines.

With the advent of x-ray micro-computed-tomography (micro-CT), the microstructure of porous systems can be imaged and visualized, allowing phase segmentation and direct characterization. Typically, porous samples of $O(\text{cm}^3)$ can be imaged at a resolution of several micrometers, creating images of size 1000^3–3000^3 voxels [8]. Following image segmentation, models at the pore scale of the image can be built to directly predict, e.g., fluid flow [9], electrical resistivity [10], and reactive transport [11]. The segmented images can also be used directly for materials characterization and to detect material defects [7]. The resolution of the image is intricately tied to the accuracy, both in a numerical-model sense and in the ability to resolve key small-scale features [12]. The field of view (FOV) of the image controls the ability of the model to capture larger-scale features and therefore its ability to predict realistic engineering relevant properties at scales of interest, e.g., effective permeability [13]. However, there are inherent

*samuel.jackson@csiro.au

FOV and resolution trade-offs in traditional absorption-based x-ray micro-CT imaging—typically, a resolution 3 orders of magnitude below the FOV is possible [14]. With ever-increasing hardware specifications, these trade-offs are continually reducing but there are technological limits to what is achievable, especially when considering several-orders-of-magnitude separation in scale (which is common in geological media). Alternative approaches are therefore needed to fully understand, characterize, and model multiscale porous system.

Alternative approaches generally either try to create breakthrough hardware implementations or develop software- and/or modeling-based improvements. Recently, advances have been made in combining x-ray and neutron dark-field imaging using grating interferometry to allow subresolution-feature-size quantification [15]. On the software and modeling side, a common approach is to implement some sort of homogenization [16]. In this approach, the physics of small-scale phenomena are captured in an upscaled continuum manifestation through the form of an averaging law. The small-scale physics is effectively captured in the coarser large-scale model, allowing the prediction of macroscopic features [6]. In the digital-rock-physics space, researchers have recently utilized homogenization approaches to incorporate subresolution microporosity into multiscale models, allowing effective characterization of transport properties over macroscopic scales, while including subresolution impacts [17,18]. Statistics-based models have also shown promise, whereby lower-resolution images use well-resolved statistics linked to high-resolution (HR) features to model large-scale systems accurately [19].

While these approaches offer improvements over the aforementioned direct methods and increase the size (and effective resolution) of systems that can be analyzed, step-change advances are potentially possibly through the application of deep learning (DL) supported by advances in graphics-processing-unit (GPU) hardware and network architectures [8]. Since deep-learning development has been rooted in computer vision and photographic image processing, many approaches are readily suited to offer improvements for x-ray micro-CT imaging and modeling [8]. In the computer-vision community, superresolution (SR) is the classical ill-posed problem aiming to reconstruct HR images from low-resolution (LR) images, essentially trying to directly enhance image resolution beyond hardware limits. With this, coarse images taken across large FOVs could be enhanced artificially to the level required to perform accurate modeling, thus circumventing traditional trade-offs in analyzing multiscale porous systems.

Conventional SR methods include projection onto convex sets (POCS) [20,21], Bayesian analysis [22,23], and example-based [24,25] and sparse representation [26,27]. However, these conventional SR methods have drawbacks that limit their practical use; for instance, example-based approaches need to learn from large dictionary pairs at the expense of excessive computational times [28] and POCS-based approaches usually cause underconstrained solutions [29]. With the rapid development in the field of GPUs, deep-learning algorithms have since achieved state-of-the-art performance on SR reconstruction problems. DL-based SR methods aim to learn the hierarchical representation of data by an end-to-end mapping between LR and HR data. Instead of learning the dictionary mapping as per traditional SR approaches [28,30], DL-based SR methods learn the information via multiple neural-network layers implicitly [31]. Once trained, the DL networks can be used on unseen data to create SR images readily from LR images, creating large multiscale data sets for analysis. Dong *et al.* [31] have proposed a superresolution convolutional neural network (SRCNN) based on patch-based data and have achieved superior performance compared to traditional SR methods. Since then, many deep-neural-network architectures have been developed for the SR problem [32–37]. Approaches using paired (i.e., registered) training data generally achieve the most accurate results. However, as paired data are not always available, unpaired DL models have also been developed based on generative adversarial networks (GANs) [38,39], which have also shown accurate results.

There are recent examples of DL-based SR models applied to x-ray micro-CT data for digital rock analysis. Typically, pixel-wise metrics, such as the peak signal-to-noise ratio (PSNR) and the structural-similarity-index measure (SSIM), have been the primary means of monitoring model performance and assessing similarity between SR and HR images [40–42]. These works have mainly focused on the SR-reconstructed image quality itself. Unpaired GAN approaches to improve micro-CT image resolution have been developed in Refs. [43,44], the results being validated using petrophysical-property predictions, such as permeability and porosity, as well as geometrical metrics, such as the Euler characteristic. All of these approaches (apart from Ref. [44]) have used LR images created from downsampled HR images, not through direct optical manipulation with the micro-CT hardware. The true level of noise transferral across scales is difficult to assess directly when using images generated from one another, even if noise is added. Although Ref. [44] has used optically generated HR data for training, their GAN approach has been validated on unpaired data. A SR method using paired LR and HR data obtained using hardware-based optical magnification has been demonstrated in Ref. [45]. The authors also compared against artificially downsampled LR data across a number of petrophysical and geometric measures, demonstrating the ability of deep-learning methods to produce physically realistic SR images.

Three critical components lacking from these previous studies are: the development and testing of the

deep-learning network on imperfect HR data (e.g., with detector and/or reconstruction artifacts); direct experimental validation of the SR image properties (i.e., not just numerical-simulation verifications); and the application of the approach to a truly multiscale system, involving heterogeneity and testing data different than the original training data. In this work, we tackle these components directly, using data from high-quality multiphase-flow experiments performed on multiple samples, imaged at varying resolution with some image defects presents. The experimental data set is from Ref. [6] and utilizes two distinct Bentheimer sandstone cores of diameter 1.25 cm and length 6–7 cm, with varying centimeter-scale layered heterogeneities. It consists of 6-μm-resolution images of the whole cores in dry, brine-saturated, and partially saturated states during steady-state decane-brine fractional-flow experiments with continuous pressure measurements. We enhance the data set by performing additional x-ray imaging of the cores in their dry state at varying resolution using optical magnification, creating paired data in four subvolumes at 2-, 6-, and 18-μm resolution.

The data are used to develop and train a 3D enhanced deep-superresolution (EDSR) convolutional neural network, based on the original two-dimensional (2D) implementation in Ref. [35]. Distinct from previous work, we use a single subvolume to train the network but test the network on unseen data from other subvolumes in different samples, with regions of varying microstructure. The unseen data are from a similar rock type (sandstone) as the training set but have distinct microstructure and flow properties. We validate the SR results using conventional image metrics and pore-network model (PNM) flow simulations, comparing to the paired ground-truth HR data. We do this across multiple image-processing realizations, giving an unbiased comparison between the results [46,47]. We then apply the trained EDSR network to generate whole-core images of the full samples, allowing us to analyze key multiscale features that impact the large-scale flow. We perform the EDSR SR generation in parallel, on approximately 1000 distinct volumes of size 1000^3 voxels for each core, creating whole-core images of total size approximately $6000 \times 6000 \times 32000$ voxels, significantly larger than direct imaging would permit. The HR subvolume images (1000^3 voxels) are used with the PNM to generate spatially varying petrophysical properties across the samples. We utilize the network-modeling approach to alleviate the direct-modeling computational costs, which would be infeasible for approximately 1000 distinct volumes of size 1000^3 voxels, even on supercomputing clusters. The petrophysical properties are combined to create 3D continuum models, which we use to simulate the experiments directly. We can then compare measured pressures and 3D saturations at varying scales directly to the experiments, thus providing a true validation of the multiscale performance of the deep-learning method. The modeling approach is predictive, in the sense that continuum properties are directly generated from pore-scale models, meaning that the approach is calibration free and deterministic, leaving significantly less ambiguity compared to other approaches.

The main contribution of this work is the development of a fully tractable and predictive methodology to model multiphase flow in heterogeneous porous systems by coupling deep learning, pore-network modeling, and micro-CT imaging. The advancements from previous works are threefold; (1) we develop an improved deep-learning method for superresolving 3D LR data, which is applicable to micro-CT images with common hardware and/or reconstruction defects; (2) we develop an integrated workflow from image acquisition to modeling that allows accurate multiscale analysis of heterogeneous systems that are otherwise intractable; and (3) we verify and validate the approach with numerical and experimental data, in samples of different heterogeneous structure across a range of test conditions. Overall, the presented methodology could be applied to any type of natural or engineered porous system with multiscale heterogeneity where the optimization of flow and transport is of upmost importance.

The paper is organized as follows:

(1) We first present the workflow methodology, including image processing, deep-learning, pore-network modeling, and continuum modeling.

(2) We then present results comparing various metrics of the generated SR images to the ground-truth HR images.

(3) We finish by using the trained EDSR network to generate SR images of the whole-rock samples, which in turn are used to generate continuum models. Continuum-model simulations are then compared to experimental results across multiple flow regimes.

II. METHODOLOGY

A. Overview

The combined multiscale characterization and modeling workflow is summarized in Fig. 1. It comprises image acquisition and training and testing of the deep-learning algorithm, followed by application and creation of a 3D continuum model, concluding with continuum-scale multiphase-flow simulations and comparison to experiments.

We demonstrate the methodology on two distinct Bentheimer rock cores—referred to throughout as cores 1 and 2—which have previously undergone extensive experimental and modeling work in Refs. [6,48]. The cores have diameter 12.35 mm, lengths 73.2 mm and 64.7 mm, core-averaged porosities of 0.203 and 0.223, and permeabilities of 1.636 D $\pm$ 0.025 D and 0.681 D $\pm$ 0.006 D for cores 1 and 2, respectively. Core 2 has a clear low-permeability lamination occurring at approximately two thirds of the

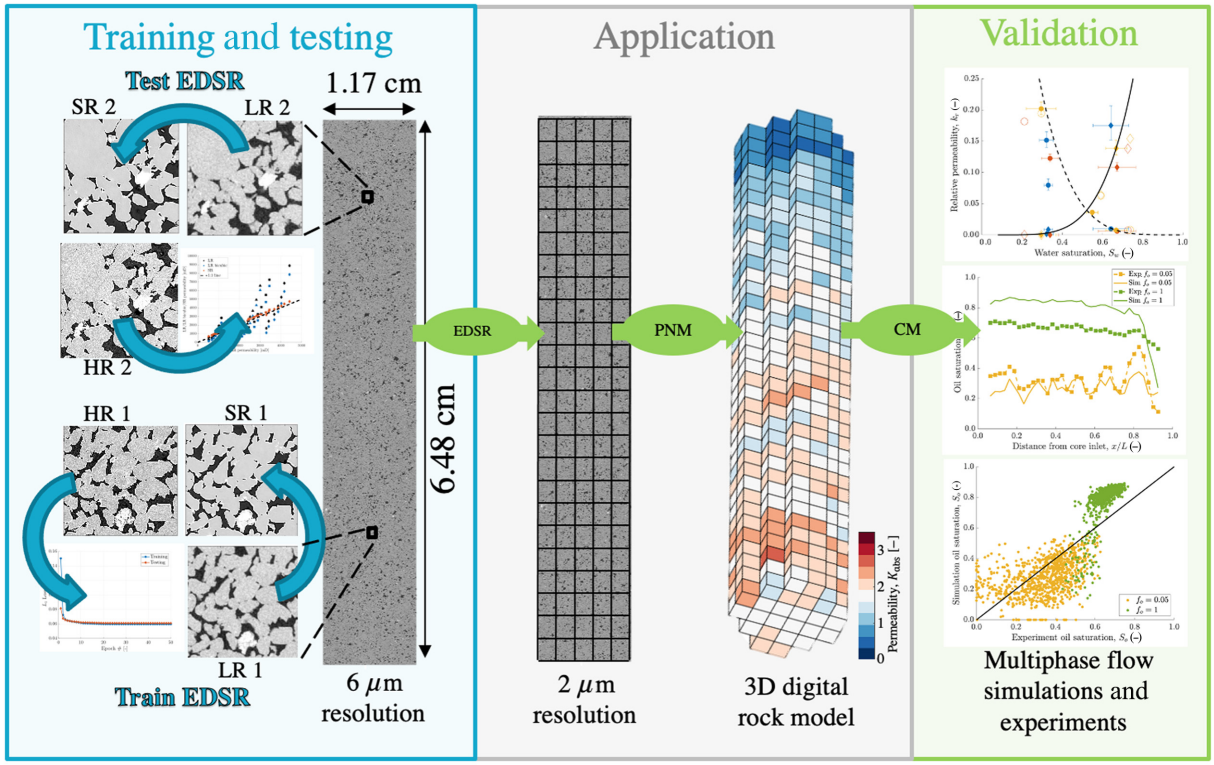

FIG. 1. A summary of the multiscale characterization and modeling workflow, flowing from left to right. First, the EDSR network is *trained and tested* on paired LR and HR data to produce SR data that emulate the HR data. Second, the trained EDSR is *applied* to the whole-core LR data to generate a whole-core SR image. A pore-network model (PNM) is then used to generate 3D continuum properties at representative-elementary-volume (REV) scale from the postprocessed image. Finally, the 3D digital model is *validated* through continuum modeling (CM) of the multiphase-flow experiments. Note that here we show the workflow using core 1. For core 2, we do not perform any extra training—we use the same trained EDSR model and apply this straight to the unseen LR data.

total core length, whereas core 1 has a general fining of grains toward the outlet of the core, creating a reduction in porosity [6].

The experimental data set from Ref. [6] consists of 6-μm resolution images of the whole cores in dry, brine-saturated, and partially saturated states during steady-state decane-brine fractional-flow experiments for both drainage and imbibition coinjections. Here, we focus solely on the drainage cycle of the experiments; multiscale modeling of the imbibition evolution and trapping is the focus of ongoing work. We compare to the more complete experiments 2 and 3 in Ref. [6], which were performed on cores 1 and 2, respectively. The experiments were performed at 1.5-MPa pore pressure, at a temperature of 30 °C. Brine and decane (oil) were coinjected at a fixed total flow rate of 0.1 ml min^{-1}. The fractional flow of decane was varied in the drainage cycle with the values $f_o = 0$, 0.05, and 1 for core 1 ("exp 2") and $f_o = 0$, 0.05, 0.5, and 1 for core 2 ("exp 3"). Each fractional flow was run until steady state was achieved in the pressure and saturation profiles, generally taking over 1 day. At each steady state, whole-core images were taken. Saturations were reconstructed from millimeter to centimeter scale and core average relative permeabilities were calculated from measured pressure drops across the sample. We use these measures in the final continuum-scale modeling and validation.

We perform extra imaging of the cores to create paired LR and HR data in order to train and test the deep-learning algorithm. We image two subvolumes for each core, at locations one third and two thirds of the way along the core length, at resolutions of 2 μm and 6 μm. The same Zeiss Versa 510 x-ray micro-CT scanner and protocol is used as in Ref. [6]—we use a flat-panel detector for the 6 μm image and a 4× optical-microscope objective for the 2-μm image. Precise energies, projections, and binning information can be found in the Supporting Information of Ref. [6].

B. Image processing

The acquired LR and HR tomographic images are first reconstructed using Zeiss reconstruction software, correcting for beam-hardening artifacts and center shift of the sample. The corresponding 2-μm and 6-μm images are then registered using normalized mutual information and cropped to remove edge artifacts. The final image sizes are

225^3 and 675^3 voxels for the 6-μm- and 2-μm-resolution scans, respectively. The images are then normalized to have consistent grayscale values [6]:

$$\mathrm{CT}_{\mathrm{new}} = S(\mathrm{CT}_{\mathrm{old}} + O), \tag{1}$$

where the scaling factor S and the offset O are given by

$$S = \frac{\mathrm{CT}_{\mathrm{ref2}} - \mathrm{CT}_{\mathrm{ref1}}}{\mathrm{CT}_{\mathrm{pk2}} - \mathrm{CT}_{\mathrm{pk1}}}, \; O = \frac{\mathrm{CT}_{\mathrm{ref1}}}{S} - \mathrm{CT}_{\mathrm{pk1}}. \tag{2}$$

Here, $\mathrm{CT}_{\mathrm{ref1}}$ and $\mathrm{CT}_{\mathrm{ref2}}$ are the reference values for the pore and grain space (chosen as 2000 and 10 000, respectively) and $\mathrm{CT}_{\mathrm{pk1}}$ and $\mathrm{CT}_{\mathrm{pk2}}$ are the measured peak values for the minimum and maximum grayscale phases present in the image. $\mathrm{CT}_{\mathrm{pk1}}$ and $\mathrm{CT}_{\mathrm{pk2}}$ are found from the grayscale histogram using a MATLAB in-house peak detection algorithm. We then convert the images from 16 bits to 8 bits:

$$\mathrm{CT}_{\mathrm{8bit}} = \frac{\mathrm{CT}_{\mathrm{16bit}} - \mathrm{CT}_{\mathrm{min}}}{\mathrm{CT}_{\mathrm{max}} - \mathrm{CT}_{\mathrm{min}}}, \tag{3}$$

where $\mathrm{CT}_{\mathrm{16bit}}$ is the input voxel value and $\mathrm{CT}_{\mathrm{min}}$ and $\mathrm{CT}_{\mathrm{max}}$ are the related extremes determined from the grayscale histograms, here taken as 0 and 2×10^4, respectively. At the end of this processing, we have two subvolumes of normalized registered LR and HR data for cores 1 and 2, giving four subvolumes in total at two resolutions. We note that we also obtain very-low-resolution (VLR) data at 18 μm for the subvolumes, using the same workflow. These data are not used here, since the whole-core images are at 6 μm, but they are included in the data share (see the end of the main text) for further work.

C. Deep learning

To train the deep-learning algorithm, we only use the paired data from core 1 subvolume 1, leaving the other three subvolumes for validation. Image patches are extracted from the LR and HR data with size 30^3 and 90^3 voxels, respectively, through an overlapping moving window (15- and 45-voxel overlap for each patch, respectively). This creates 8000 patches, from which we use 6400 patches for training and 1600 patches for validation in a 80:20 Pareto split. Figure 2(b) shows a 2D slice of a typical training image patch at low and high resolution. The patch size is chosen to cover the largest typical pores present in the Bentheimer samples of $O(100\ \mu\mathrm{m})$.

We employ a 3D EDSR model as our deep-learning algorithm, shown in Fig. 2(a). The EDSR encompasses a sequence of convolutional layers, residual blocks [49], and an upsampling module. Along with skip connections in the residual blocks, the EDSR can alleviate gradient vanishing

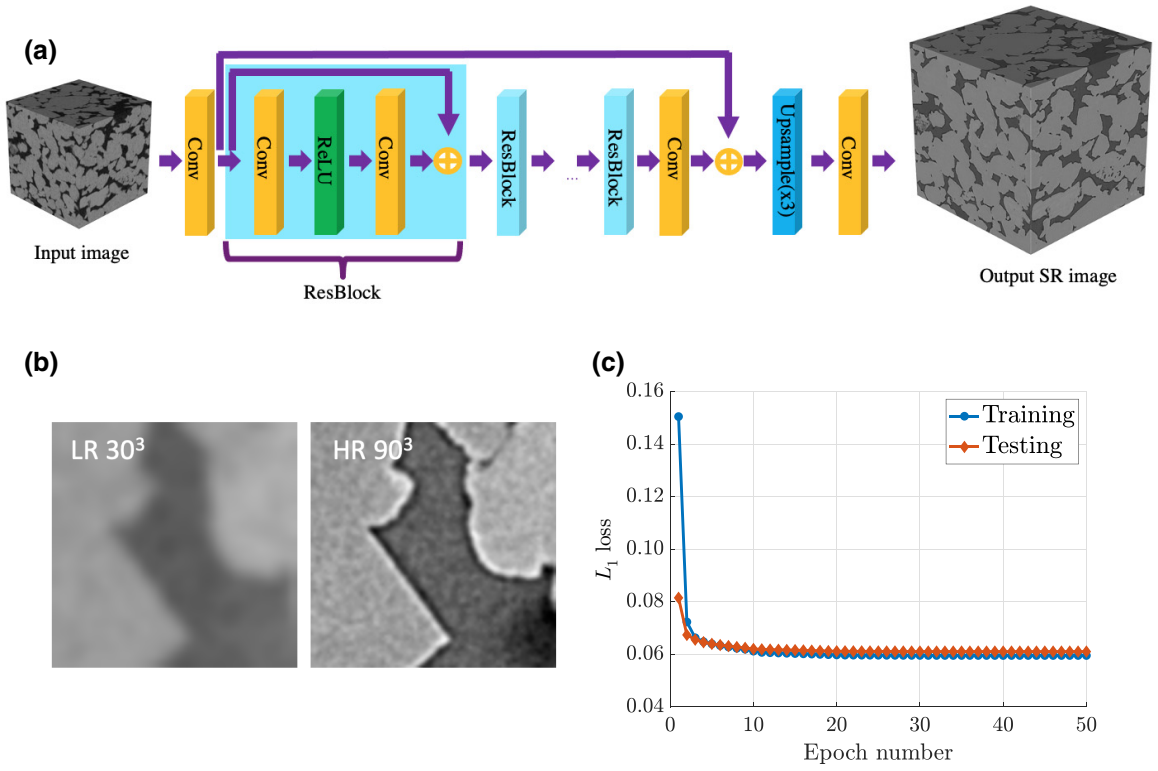

FIG. 2. The deep-learning workflow and testing and training. (a) The EDSR network architecture. (b) Example testing images: the LR image is at 6-μm resolution and the HR image is at 2-μm resolution. (c) The L_1 loss function for the EDSR network training and testing over 50 epochs.

or exploding problems. We use a modified version of the original 2D EDSR structure from Ref. [35]. Instead of using the pixel-shuffle upsampling methods proposed in Ref. [34], we utilize trilinear upsampling in our 3D implementation. In addition, we also reduce the numbers of residual blocks and filters (12 residual blocks and 24 filters in each convolutional layer) appropriately to improve the computational efficiency and in an effort to reduce the overfitting of artifacts that is apparent in the HR micro-CT image, specifically ring and beam-hardening artifacts. These are discussed in more detail in Sec. III A.

We utilize the Adam optimization algorithm for training [50], with a batch size of 32 and total epochs of 50, chosen through user experience in the training process. The learning rate is initially set to 1×10^{-5} and decreased tenfold every ten epochs to consolidate the training process. The $L1$ loss metric is utilized to train and monitor the EDSR network:

$$L_{1,\mathrm{loss}} = \sum_{i=1}^{n} \left| \mathrm{CT}_{i,\mathrm{HR}} - \mathrm{CT}_{i,\mathrm{SR}} \right|, \tag{4}$$

where $\mathrm{CT}_{i,\mathrm{HR}}$ and $\mathrm{CT}_{i,\mathrm{SR}}$ are the pixel grayscale CT values for the HR and the generated SR images, respectively. The training and testing $L_{1,\mathrm{loss}}$ is shown in Fig. 2(c), highlighting convergence to a low loss (3 times reduction from the initial) after approximately ten epochs. The training is implemented in PYTORCH using a NVIDIA GeForce RTX 2080Ti.

Once trained, the EDSR network can be utilized to generate SR images with a 3 times increase in resolution from any input LR images (for other integer factors, e.g., 2 times and 4 times, a new network has to be trained on corresponding data). We utilize the EDSR to generate corresponding SR images for the unseen LR images from core 1 subvolume 2 and for core 2 subvolumes 1 and 2. With corresponding HR data, these images can be directly evaluated to assess the efficacy of the EDSR network in producing an SR image that emulates the HR image. As a further comparison, we also generate a HR image using a simple 3D cubic interpolation of the LR image to the required 3 times resolution, with the result labeled "cubic." This allows comparison with common polynomial-interpolation methods that can be employed to increase the resolution of an image without using any prior knowledge of the image or trained weights. This also acts as example of what a simple resolution enhancement can achieve when performing network extractions and flow simulations, which are often mesh dependent.

To quantitatively compare the paired LR, cubic, SR, and HR images across the samples, we use a mix of image analysis and flow simulations performed with pore-network modeling. To this end, the images must be segmented into binary pore and grain phases, so that pore networks can be extracted.

Due to the differing noise levels in the images, it is useful to filter the images to a common level, such that subsequent segmentations are comparable. It is well known that filtering and segmentation operations in image processing can be highly user specific and biased [46] if objective measures of the output are not used. We perform the filtering operation objectively using the SSIM [51]. Since the SR image generated from the EDSR network is essentially filtered in the ResBlocks (see Fig. 5 below), we filter the LR, cubic, and HR images to a similar level, using the SR image as a reference. To compare and optimize the resultant output to have similar filtering levels, we use the SSIM between the images and the SR image, given by

$$\mathrm{SSIM}(x,y) = \frac{\left(2\mu_x\mu_y + C_1\right)\left(2\sigma_{xy} + C_2\right)}{\left(\mu_x^2 + \mu_y^2 + C_1\right)\left(\sigma_x^2 + \sigma_y^2 + C_2\right)}, \tag{5}$$

where μ_x, μ_y, σ_x, σ_y, and σ_{xy} are the mean, standard deviation, and covariance between images x and y. C_1 and C_2 are regularization constraints for regions with a mean or standard deviation close to zero: for the images shown here, they are given by $(0.01d)^2$ and $(0.03d)^2$, where d is equal to the dynamic range of 255. To filter the LR, cubic, and HR images, we use a nonlocal means filter with varying filter strength [52]. The search-window and comparison-window sizes are set to maximize the SSIM with 11 and 5 voxels, respectively, and increased 3 times for the HR images.

In Fig. 3(a), we compare the SSIM for the cubic and HR images to the SR image for varying filter strengths, across all four subvolumes. We cannot directly compare the LR image due to the image-size mismatch with the SR image. Nonetheless, we see that the HR image shows a greater similarity with the SR image across all filter strengths than the corresponding cubic image. In the figure, we show the optimum filter strength for both cases, which is chosen to maximize the SSIM across all subvolumes. We use these filtering parameters for all images in subsequent processing.

Previous studies comparing image-enhancement methods have typically used a single user-defined segmentation threshold, based, for example, on the "optimal balance between over- and underestimating connectivity" [45]. This makes objective comparison between outputs difficult. Here, we use a range of threshold values, in the spirit of Refs. [47,48,53], and compare the results quantitatively across the range, to indicate the sensitivity and absolute variations. We use a simple threshold segmentation method, with the base-threshold level chosen as the minimum between the pore and grain peaks in the grayscale histograms [see Fig. 3(b) [48]]. This minimum (value 117) is selected as the average minimum for the LR and HR training images and is close to the minima for all images [SR also; see Fig. 3(b)]. We segment the pore space

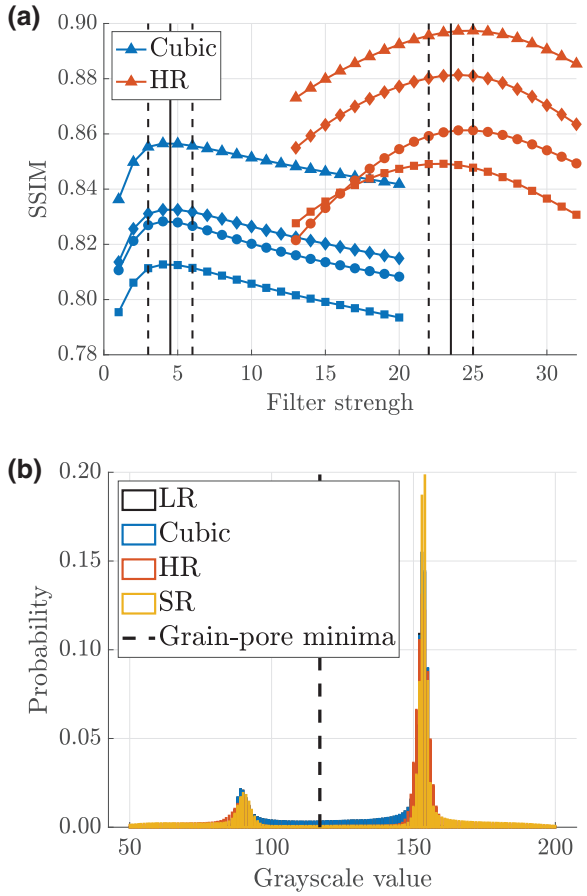

FIG. 3. The image-processing steps to allow quantitative segmentation and flow comparisons. (a) The structural-similarity-index measure (SSIM) of the filtered cubic and HR images compared to the SR image. The various symbols refer to the subvolumes: triangles, core 1 subvolume 1; diamonds, core 1 subvolume 2; squares, core 2 subvolume 1; circles, core 2 subvolume 2. The optimum filter strength is shown as the solid black lines for the cubic and HR images (the dashed lines highlight the maxima). (b) Histograms of grayscale values for the filtered core 1 subvolume 1 image, showing the base segmentation threshold (minima between grains and pore = 117 grayscale value) and overlapping distributions of the normalized images.

based on this threshold and vary it from −15% to +15% in 5% increments, creating a total of seven segmentations for each subvolume.

D. Pore-network modeling

The segmented LR, cubic, HR, and SR images are used in a pore-network modeling workflow to predict key petrophysical parameters. Pore networks are extracted from the binary images using the conventional network-extraction tool from PNEXTRACT [54], an updated version of which has been presented earlier in Ref. [55]. A distance map of each voxel to its nearest solid voxel is used to construct a medial surface of the pore space with a maximal sphere hierarchy; each sphere has a radius equal to the distance map. An iterative scheme then removes overlapping nested maximal spheres along the medial surface. This results in a set of voxels on the medial surface that have a maximal sphere and connectivity with neighboring points, representing the pore-space morphology. A watershed segmentation of the distance map is then used to assign each voxel (and neighbors) on the medial surface to a unique pore body, with the joining faces between bodies defining the connecting throats.

The resulting pore network is used in flow simulations using the PNFLOW package from Ref. [56], an updated version of the original algorithm from Ref. [57]. The conventional network extraction and flow simulation has been validated in previous works [48,53], as well as the more complex generalized network-modeling approach [58]. For the flow modeling here, pore throats are assigned a shape factor based on the underlying pore-space geometry:

$$G = \frac{R^2}{4A}, \tag{6}$$

where R is the inscribed radius of the maximal sphere and A is the cross-section area of the throat [53]. The pore bodies use a shape-factor average from the connected throats, weighted by the connected cross-section area of the throats. Based on G, the network elements have triangular, square, or circular cross sections, depending on the following criteria [54,56,57]:

$$0 \le G \le \frac{\sqrt{3}}{36}, \quad \text{triangular}, \tag{7}$$

$$\frac{\sqrt{3}}{36} < G \le 0.07, \quad \text{square}, \tag{8}$$

$$0.07 < G, \quad \text{circular}. \tag{9}$$

Quasistatic capillary-dominated drainage flow is simulated in the network elements using fluid-interface force balances with the Mayer-Stowe-Princen method [59]. All throats at the network inlet are assumed to be filled with nonwetting phase. In each displacement step, a wetting and nonwetting phase pressure are prescribed to give a defined capillary pressure, $P_c = P_{nw} - P_w$. The throats and pores are then drained in order of increasing capillary entry pressure controlled by the network-element shapes and contact angles. In the strongly water systems considered here, we assume a contact angle of 45° to be comparable to mercury-intrusion experiments and drainage-flow experiments [6]. Arc menisci can form due to small wetting layers in the polygonal elements, which require complex entry-pressure calculations, given in Refs. [57,59]. Once all available and accessible elements are filled, the network saturation can be found based on the invaded-network volume, giving a macroscopic $P_c(S_w)$. Incrementing the

nonwetting phase pressure in steps until the irreducible saturation simulates a full drainage cycle.

At each equilibrium stage, connected-pathway single or multiphase transport can be simulated through the network. Both hydraulic (absolute and relative permeability) and electrical (resistivity, formation factor) properties are calculated. Conservation of flux (electrical or mass) Q is imposed at each pore body p through adjoining throats t:

$$\sum_{t\in p} Q_t^\alpha = 0, \tag{10}$$

where α is the fluid phase. The local flux between adjoining pores i and j is given by

$$Q_{ij}^\alpha = \frac{g_{ij}^\alpha}{L_{ij}}\left(\Phi_i^\alpha - \Phi_j^\alpha\right), \tag{11}$$

where g_{ij}^α is the conductance for phase α between pores of center separation L and Φ is the potential. Equations (10) and (11) can represent both fluid or electrical flow, by changing the potential and phases accordingly. The conductance is the harmonic mean of the two pore-body conductances and the connecting throat element. The hydraulic conductance for a single element is calculated analytically using Poiseuille's law for single-phase flow, based on the element geometry [57]. For multiphase flow, corner and layer flows can occur—here, we use empirical conductances based on the flow geometry, validated with laminar Stokes flow simulations [57]. For electrical conductivity, we only consider the water-phase conductivity at fully saturated conditions. The electrical conductance for an element is given by the bulk water conductance multiplied by the element cross-section area.

A linear set of equations for pore-body potentials can be created from Eqs. (10) and (11), with appropriate potential boundary conditions at the inlet and outlet faces [constant potential difference of 1 Pa (pressure) or 1 V (electrical)] and zero-flux boundaries on the other faces. The system can be formed for single-phase flow, multiphase connected-pathway flow, and electrical flow. Solving this system, the inlet and outlet fluxes can be reconstructed by summing across the appropriate elements. With this, the absolute permeability, relative permeability, and formation factors can be calculated:

$$K = \frac{\mu_w Q_{\mathrm{SW}} L}{A\left(\Phi_{\mathrm{inlet}} - \Phi_{\mathrm{outlet}}\right)}, \tag{12}$$

$$k_{r,\alpha} = \frac{Q_\alpha}{Q_{\mathrm{SW}}}, \tag{13}$$

$$F = \frac{Q_{\mathrm{SW}}^e L}{\sigma_w A\left(\Phi_{\mathrm{inlet}}^e - \Phi_{\mathrm{outlet}}^e\right)}, \tag{14}$$

where μ_w is the water viscosity, Q_{SW} is the fully saturated water flux, Q_α is the phase fluid flux at intermediate saturation, Q_{SW}^e is the electrical flux in the water-saturated system, $\Phi_{\mathrm{inlet}} - \Phi_{\mathrm{outlet}}$ is the pressure drop across the system, $\Phi_{\mathrm{inlet}}^e - \Phi_{\mathrm{outlet}}^e$ is the electrical-potential drop across the system, and σ_w is the bulk-water electrical conductivity.

We use bulk-fluid properties equivalent to those in the brine-decane flow experiments described previously. The fluid viscosities are 7.83×10^{-4} Pa s [60] and 8.03×10^{-4} Pa s [61], and the densities are 1023.2 kg m^{-3} [62] and 723.8 kg m^{-3} [61], for the brine and decane, respectively. We use an equilibrium contact angle of 45° and an interfacial tension of 51 mN/m. We use a residual saturation of brine, interpreted from the experiments as $S_{\mathrm{wirr}} = 0.08$, and an electrical resistivity of brine as 1.2Ωm.

The petrophysical properties calculated using the pore-network model are used for verification of the deep-learning image enhancement. The results are compared across the different segmentations for each LR, cubic, HR, and SR subvolume, allowing for direct quantitative verification.

E. Continuum modeling

Following verification of the deep-learning enhancement (e.g., training, testing, and PNM verification), we further validate the approach by performing continuum-scale simulations of the aforementioned experiments. To do so, we construct digital models of the whole-rock cores, populated with petrophysical properties that vary spatially at the representative elementary-volume scale.

The LR whole-core images of cores 1 and 2 are first subdivided into representative elementary volumes. The sizes of these volumes have been extensively researched in Ref. [6], generally showing that cubic side lengths of > 1.5 mm are required to reach representative volumes, where parameter fluctuations drop to with 5% of the large-scale variance. We choose the same LR-subvolume size as per Refs. [6,48]—$316 \times 316 \times 300$ and $316 \times 316 \times 318$ voxels for cores 1 and 2, respectively, ensuring $>$ 1.5 mm in side length. Following this, the EDSR network detailed previously is used to enhance the LR-subvolume images, increasing the resolution by a factor of 3. This creates SR subvolumes of size $948 \times 948 \times 900$ and $948 \times 948 \times 954$ voxels at 2-μm resolution, for cores 1 and 2, respectively.

The LR and SR representations of the whole-core images are next filtered and segmented, in a similar vein to the imaging processing (see Sec. II B). The filtering protocol is identical but we segment based on calibration with an externally measured total porosity, derived through medical x-ray CT imaging. The threshold value from the LR and SR images is chosen so that the segmented porosity matches that of the medical-CT-derived value, shown in Fig. 4. The high-threshold (HT) value shows

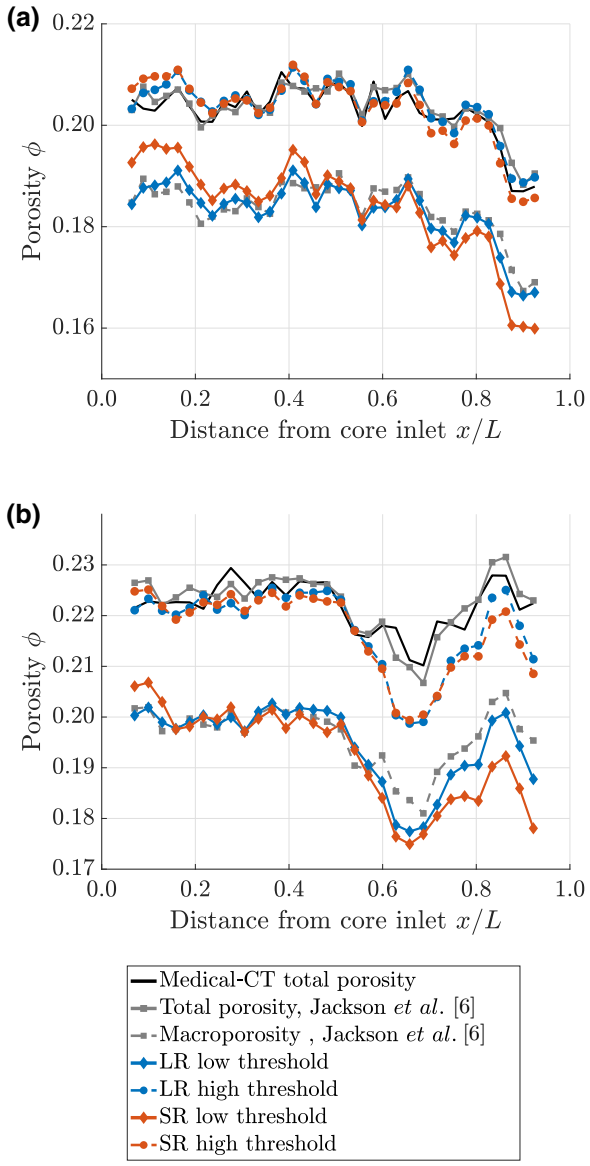

FIG. 4. Porosity profiles for (a) core 1 and (b) core 2 for the LR and SR images at two different segmentation thresholds—high-threshold (HT) and low-threshold (LT)—chosen to match the medical-CT-derived total porosity and the macroporosity from earlier analyses [6], respectively. The plot legend is shown at the bottom. The specific LT and HT threshold segmentation values are as follows: core 1 LR, 117/122; core 1 SR, 104/117; core 2 LR, 118/123; core 2 SR, 104/119.

the corresponding match for the LR and SR images to the medical-CT value, along with a previous "total-porosity" segmentation from Ref. [6]. The slice average porosities from all four images match well. Small discrepancies between the micro-CT segmented images are due to feature representation and the segmentation choice in Ref. [6], which uses a watershed segmentation.

As there is likely oversegmented pore space in each image (due to the resolution limit and the matching of a "total porosity" measured from medical-CT imagery), we perform a further segmentation at a lower threshold (LT). This threshold is chosen to approximate the macroporosity in the core from Ref. [6]. This lower threshold removes intermediate gray regions from the pore space, e.g., clay regions or partial-volume effects at pore-grain boundaries. It can give a more representative pore space for low-capillary-number flow simulations, since the nonwetting fluid does not drain clay-bound microporous regions. The LT segmentations shown in Fig. 4 match the results from Ref. [6] well and give an estimate of the macroporosity of each system. In each case, the clay content in the core is approximately 0.02–0.03 in porosity, in line with physical measures of Bentheimer sandstone [63]. The absolute segmentation threshold values are slightly different for the LR and the SR images due to different feature representation and filtering in each image. Although the filtering is optimized to give the highest SSIM, the noise distribution is inherently different between the different images.

The LT- and HT-segmented subvolumes for the LR and SR whole-core images are then passed to the pore-network modeling workflow as detailed in the previous section. Petrophysical properties are predicted for each subvolume—namely, porosity, permeability, relative permeability, and capillary pressure—using the same fluid properties as before. This is performed in a highly distributed manner, making use of parallel computing architecture—each subvolume is distinct and can run independently.

With the known image and subvolume geometry, we create a 3D model of each core with the subvolume petrophysical properties defined uniquely for each cell in the model. The model forms the base to conduct continuum-scale multiphase simulations using the approach developed by the authors and previously presented in Refs. [6,48,64,65]. We note that each 3D cell (of cubic side length approximately 1.5 mm) in the model has unique distinct petrophysical properties deterministically predicted from the underlying image pore network; there is no calibration or "history matching" performed.

With the 3D model defined, we numerically solve conservation of mass and momentum (the two-phase Darcy's law) using the fully implicit isothermal immiscible multiphase-porous-media flow simulator CMG IMEX^{TM}. Constant fluid properties and temperatures are used throughout the simulations. We use boundary conditions equivalent to those in the experiment—zero flux normal to the outer diameter of the core, a constant-volume flux at the inlet face, and a constant pressure at the outlet face. We vary the inlet flux to match the experimental fractional flows and run the simulations for the same time periods until steady state is achieved. We can then compare the resulting saturations in each cell to those in the experiment on a 1:1 basis, as well as core-averaged pressure drops in the form of absolute and relative permeability.

III. RESULTS

Here, we present results from the multiscale characterization and modeling workflow. We first evaluate the performance of the deep-learning algorithm in generating realistic SR images from LR images, using direct image comparisons and pore-network modeling. We follow this verification exercise with validation using whole-core continuum simulations to compare directly to experiments across a variety of conditions.

A. Pore-scale results

We first discuss the pore-scale efficacy of the workflow. The first slice of the LR, cubic, HR, and SR images for core 1 subvolume 2 and core 2 subvolume 2 are shown in Fig. 5. Only core 1 subvolume 1 is used in the training and testing of the deep-learning algorithm; the images in Fig. 5 are therefore completely unseen. Further image comparisons are shown in Figs. S1–S3 in the Supplemental Material [66]. We show the raw images as well as filtered images, which highlight the high filtering similarity that is achieved between the SR and HR images [e.g., Eq. (5)]. In Fig. 5, we see that the SR image, generated through the EDSR network, is able to reproduce many of the sharp angular features apparent in the HR image, highlighted by the blue-circle regions. The LR and cubic images have much smoother feature representations, especially after filtering to the same level as the SR image. Upon segmentation, features are generally more rounded; the sharp grain-pore contacts typical of the Bentheimer sandstone are somewhat lost.

As well as sharper grain-pore contact features, high-frequency features are also significantly better represented in the SR image. Small pores and connecting throats are more resolved; this is apparent even when comparing to the cubic image (at 2-μm resolution), which is not able to capture the same detail. The EDSR learns a deeper mapping from the LR to HR image than a polynomial interpolation, using higher-level information such as the image gradient, which improves small-feature representation. This is particularly important for the overall connectivity in the domain and the subsequent pore-network extraction. Small disconnected regions [such as that shown in Fig. 5(a), blue circle] could be wrongly attributed to a different pore and may not be connected to the main flow path, leading to inaccuracies in flow simulation. In general, the SR image appears more connected than the LR or cubic images, in line with the HR image.

We see that the contrast between features is also higher in the SR image compared to the LR and cubic images. This is visible in the blue circle in Fig. 5(b), whereby intragranular porosity is more clearly visible and is retained upon segmentation in both the HR and SR images. Further analysis of the core 2 subvolume results in Fig. 5(b) (and in the Supplemental Material [66]) reveals the ability of the EDSR to learn specific mineralogy aspects of the images. Core 2 features bright patches of highly attenuating iron-oxide deposits in the form of hematite (approximately 9 times more attenuating than quartz [67]). These also appear in the visible spectrum as a distinct red color. These iron-oxide deposits typically form around fault planes from iron-rich groundwater flow and can form between quartz grains [68]. The SR image is able to reproduce these bright patches, even though they are barely visible in the relatively dark LR image (see Fig. 5(b), red circles). These patches can reduce the overall porosity and/or permeability of the sample when in between grains and are key in the heterogeneity characterization—see the simulation results for further explanation.

The EDSR network is optimized for the micro-CT data here by reducing the number of residual blocks and filters in each layer; an optimum is manually found that produces low L_1 loss while not overfitting the data. Overfitting is clearly visible in early attempts when specific beam-hardening and ring artifacts are learnt from the HR image. These are common x-ray micro-CT imaging artifacts, due to the nonlinear attenuation of the core-holder or rock and through dead pixels, respectively. The ring artifacts are visible in some HR images here [see the central-region crop in Figs. S1(c), (g), (k), and (o) in the Supplemental Material [66]] but have not been learnt by the EDSR. This is a key attribute of the EDSR implementation and it allows our SR images to represent the true features of the HR images while removing common, and often unavoidable, imaging artifacts.

A further feature that the EDSR network learns is the grain-edge artifacts apparent in the HR image. These bright regions are due to small-angle x-ray refraction (often interpreted as "phase-contrast" artifacts) and they occur increasingly at high resolution and high energy with sharply contrasting features [69]. They are not necessarily a negative effect in dry images, since they increase contrast for segmentation; however, they can be negative if multiple (fluid) phases are present in the sample, especially if phase-contact geometry is required. These features are not learnt through overfitting, since they are ubiquitous in the HR image here; they could be removed somewhat with phase-contrast-removal techniques.

It is worth noting that in Fig. 5 we only show one segmentation result, at the base-threshold value (grain-pore minimum value 117), to give a representative view of the pore space. Although other threshold values, which are not necessarily equal to each other, may result in closer visual matches between comparison images, the base threshold shown highlights the general trends between the LR, HR, and SR images. To more quantitatively compare the images, we now discuss the results from the pore-network extractions and flow simulations.

Figure 6 shows petrophysical-property predictions from the pore-network-model extractions and flow simulations

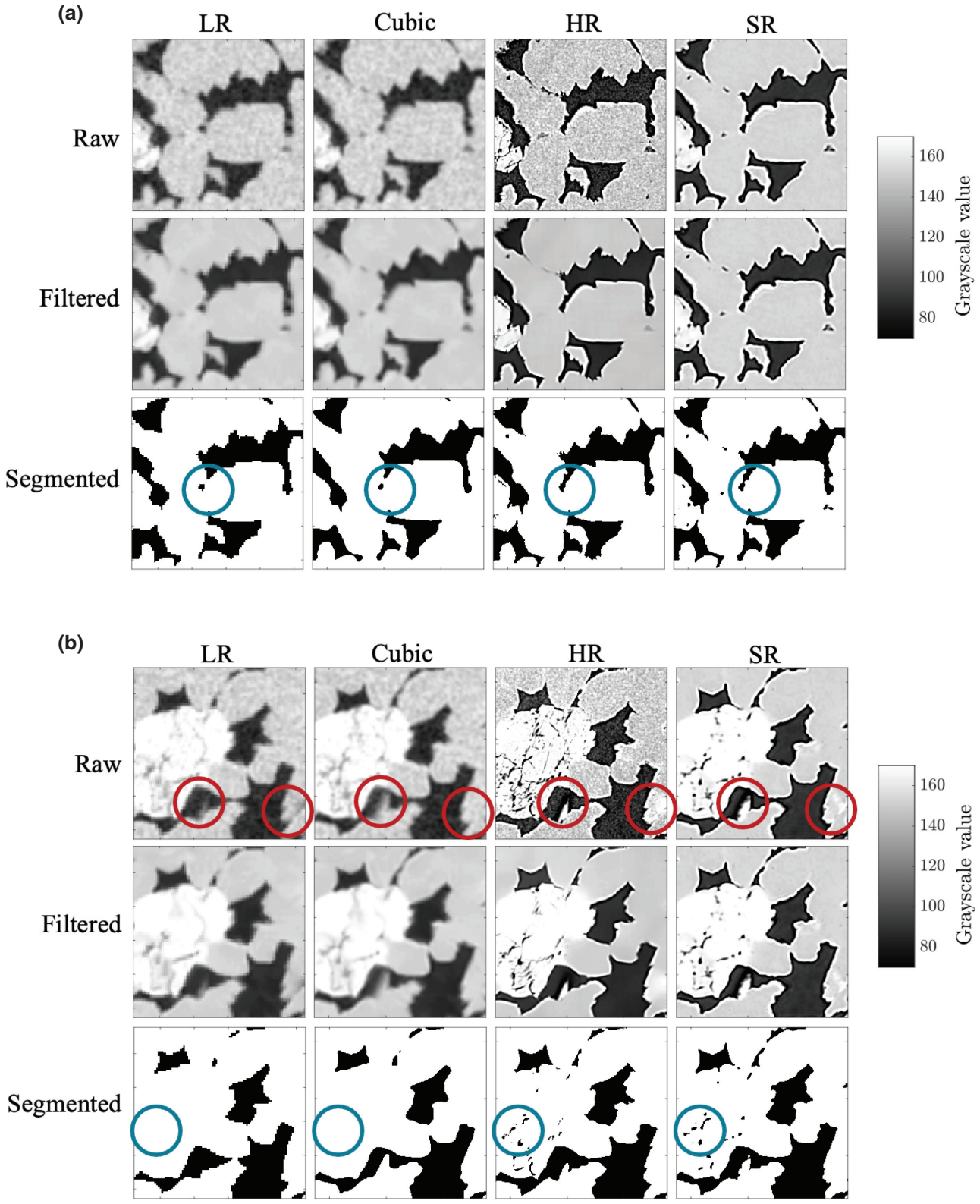

FIG. 5. Comparisons of the LR, cubic, HR, and SR images. The region shown is a 600 × 600 μm 2D crop from the first slice, centered on pixel 175/225. (a) Core 1 subvolume 2. (b) Core 2 subvolume 2. In each subfigure, the top row are raw normalized images, the middle row are filtered images, and the bottom row are the segmented images using the base-threshold-of-117 grayscale value. The columns from left to right are LR, cubic, HR, and SR images, respectively. The blue circles highlight areas of interest, showing differences between the images. The red circles show potential hematite mineral inclusions in core 2, which are also visible in many other regions (for further images, see the Supplemental Material [66]).

comparing the LR, cubic, and SR results to the HR result. In each case, seven segmentation results are shown, with the middle symbol representing the base case in each case. As the segmentation threshold is increased, the grain space is eroded and the porosity and/or permeability is increased. In general, it is clearly visible that the SR results closely match the HR results across all segmentation thresholds, closely following the unity line. This is not true for the LR and cubic results, which generally match the HR result at only one segmentation threshold, which is not equal to that of the HR image. The crossover point for the LR and cubic results with the unit line changes for each petrophysical property; therefore, it is not clear which segmentation threshold for the LR images is optimal compared to the HR image. This highlights the potential pitfalls with choosing a segmentation for a lower-resolution image based on a single criterion [46], which does not necessarily hold for other petrophysical predictions. The SR image, on the

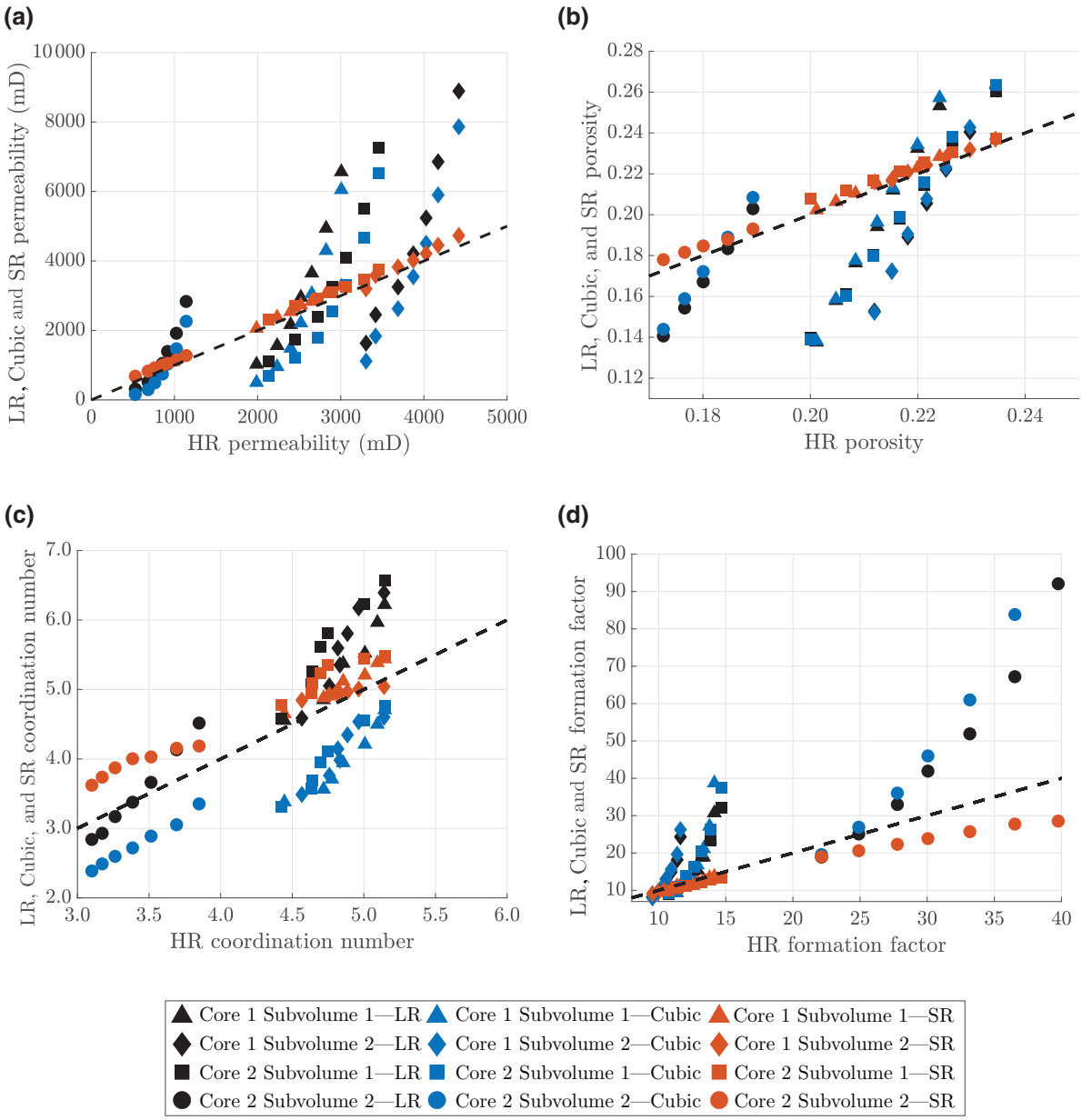

FIG. 6. Pore-network model simulations for the LR, cubic, HR, and SR images for all subvolumes. (a) Permeability. (b) Porosity. (c) Coordination number. (d) Formation factor. The dashed black 1:1 line shows the perfect correspondence of the LR, cubic, and SR data with the HR data. The legend is shown at the bottom; the symbol colors differentiate LR, cubic, and SR data, while the symbol types differentiate cores and subvolumes. Multiple points with the same color and symbol are different segmentation realizations (seven in total).

other hand, displays behavior consistent with that of the HR image across the range of segmentations. This means that given an external measurement to calibrate against, the chosen segmentation threshold should lead to consistent petrophysical-property predictions, in line with the HR image. Furthermore, the variance of the SR petrophysical properties with segmentation choice is less than the LR data, indicating that it is less sensitive to the segmentation choice itself.

Out of the four subvolumes shown in Fig. 6, core 2 subvolume 2 has the least consistent SR result compared to the HR image. This is likely due to the quantitative difference in the pore structure between that subvolume and the EDSR training subvolume (core 1 subvolume 1). The subvolume-2 location has high levels of the bright hematite mineral and a tight grain structure, with a permeability around one order of magnitude less than core 1 subvolume 1. However, the petrophysical predictions are still acceptable and generally within ± 5-10% of the HR-image results. In this work, we consciously choose to train the EDSR network on only one subvolume in one core, to highlight the small training data set that is required. The training size is chosen based on a typical representative elementary volume (REV) of Bentheimer and chosen randomly from the data sets. If the training batch was extended to include multiple regions, then conformance could likely be achieved over data with more variance. As in all deep-learning methodologies, the performance of the network is strongly tied to the quality and/or quantity of the training data set and its representativeness of the test data [8].

Multiphase-flow predictions from the pore-network models are shown in Fig. 7 for core 2 subvolume 1 (other subvolume results are shown in Figs. S4–S6 in the Supplemental Material [66]). The HR and SR results both show less variation across the different segmentation thresholds than the LR and cubic results and closely match each other generally. In particular, the capillary pressure predictions for the SR and HR images closely match the externally derived mercury-intrusion capillary pressure (MICP) data, when scaled to the correct interfacial tension (IFT) fluid pair [70]. Higher capillary pressures at $S_w < 0.2$ are better represented in the SR and HR images, due to the resolution of small pores and throats in the system. In the LR and cubic networks, these small pores are poorly resolved and hence the maximum capillary pressure that can be simulated is limited. We also see that the gradient of capillary pressure ($|dP_c/dS_w|$) in the low-capillary pressure region ($0.2 < S_w < 0.8$) is smaller for the LR and cubic networks compared to the SR and HR networks and MICP data. A low $|dP_c/dS_w|$ across a range of P_c values is indicative of a narrow pore-size distribution, where many pores are filled for small changes in P_c. The LR and cubic networks have a narrower range of pore sizes compared to the HR and SR data, as well as the real rock, misrepresenting the

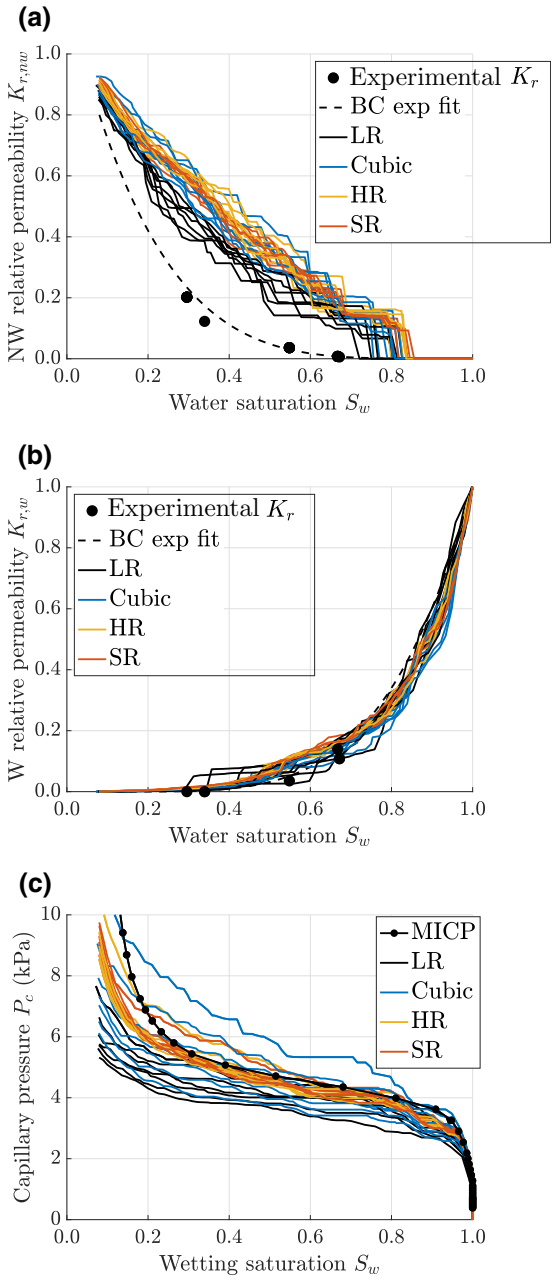

FIG. 7. Pore-network model simulation results for the LR, cubic, HR, and SR image networks of core 2 subvolume 1. Each line represent a flow simulation on one of seven different segmentation thresholds from −15% to +15% around the base-threshold-of-117 grayscale value. (a) The nonwetting relative permeability. (b) The wetting relative permeability. (c) The capillary pressure. The MICP data are from a sister core. The "Experimental K_r" data are from the core-averaged multiphase-flow experiments. Also shown is a Brooks-Corey (BC) function fit to the experimental relative permeability data, from Ref. [6].

filling process and capillary pressure in the system. Further, we see that the SR and HR networks have a better representation of the threshold capillary pressure at the first inflection point of dP_c/dS_w, where percolation across

the system starts. The more connected domains generally in these systems allow better representation of the initial filling stages.

The SR and HR relative permeability predictions in Figs. 7(a) and 7(b) also show less variance compared to the LR and cubic predictions. The wetting relative permeability is generally well predicted by all networks, with little variation across the segmentations. Since the wetting phase is connected across the domain for all saturations, the relative permeability is quite insensitive to pore-structure variations created by the different network morphologies. However the wider more connected pore-size distribution of the SR and HR networks does result in smoother transitions between filling states, with less discrete "jumps" than in the LR and cubic network. The nonwetting permeability shows larger variations across the networks, especially for the LR and cubic images at the percolation threshold. Variations in the network morphology have stronger impacts on the nonwetting percolation, especially given the pore-space heterogeneity. We note that all networks overpredict the experimental core-averaged values here. This is largely due to finite-size impacts, as the smaller-subvolume networks are more readily percolated than the whole-core system. The REV size used in this work is the same as in Ref. [6] and is chosen based on porosity and capillary pressure. It is possible that relative permeability REVs are larger. Further from this, capillary-end effects are present in the whole core (and not in the PNM), which generally reduce relative permeabilities and are present in the effective experimental K_r values; this is discussed in more detail in Sec. III B on continuum modeling. These results further highlight potential user bias when evaluating results compared to a single criterion; care must be taken to consider scale and representativeness.

Results from the other subvolumes in the Supplemental Material [66] highlight the pore-scale heterogeneity across the rock samples and the general ability of the SR networks to capture this in line with the HR networks. The varying capillary pressure compared to the base MICP data is a direct consequence of the changing pore-structure and therefore capillary pressure heterogeneity.

In this section, we rigorously validate the ability of the EDSR network to produce physically realistic SR images of the pore space from LR images. We compare common image-similarity metrics (SSIMs), visual texture, and flow simulations to the corresponding LR and HR images. Distinct from previous works [40,41,43–45,71], we develop the EDSR network in 3D and demonstrate the pore-scale validation across multiple segmentation realizations from multiple subvolumes in different samples, gaining a thorough understanding of the uncertainty. We also perform multiphase-flow validations, which are crucial for subsurface applications but are often lacking in previous, less-application-driven, studies. Further from previous work, we also validate the results with true LR and HR images obtained from optical magnification of the samples, rather than artificial up- and/or downscaling of a single image with numerical procedures. This is common in earlier verifications of the approaches but does not provide a true representation of noise transfer with scale in realistic applications [41].

B. Continuum-scale results

The verification in the previous section is performed primarily with numerical simulation; we now provide direct experimental validation of the EDSR-generated images and modeling approach. As described in Sec. II E, we use the trained EDSR network to generate HR subvolumes across the full-core samples from the LR images. These subvolumes are segmented and fed into the PNM to generate petrophysical properties and ultimately a 3D full-core-continuum model. These models permit continuum flow to be simulated by solving conversation of mass and momentum, which we compare to the experimental results from Ref. [6]. We note that the experimental results are from exactly the same rock samples and hence can be compared to the model results here in a 1:1 approach.

First, we compare core average absolute permeabilities. These are calculated in the experiments and simulation using the average pressure drop across the samples in an analogous manner to Eq. (13). Tabulated results are shown in Table I for all model realizations, with 3D permeability maps for the LR and SR LT models displayed in Figs. 8(a)–8(d) (further images are shown in Fig. S7 in the Supplemental Material [66]). We also show direct 1:1 comparisons of the voxel-permeability predictions for the LR and SR LT images in Figs. 8(e) and 8(f). For each core, we see that the SR model provides a more accurate prediction of the absolute permeability for both the LT and HT realizations when compared to the experimental average values.

We show the Dykstra-Parson coefficient, V_k, which is the ratio of standard deviation in absolute permeability

TABLE I. Single-phase flow-simulation results compared to experiments. LT and HT refer to low-threshold and high-threshold generated models, respectively.

Property	Core 1		Core 2	
	LR	SR	LR	SR
K_{abs} experiment (D)	1.636		0.681	
K_{abs} LT (D)	2.494	1.503	2.350	1.260
K_{abs} LT error (%)	52.5	−8.1	245.1	85.0
LT Dykstra-Parson coefficient, V_k	0.174	0.280	0.213	0.285
K_{abs} HT (D)	3.477	2.413	3.327	2.201
K_{abs} HT error (%)	112.6	47.5	388.5	223.2
HT Dykstra-Parson coefficient, V_k	0.152	0.202	0.202	0.221

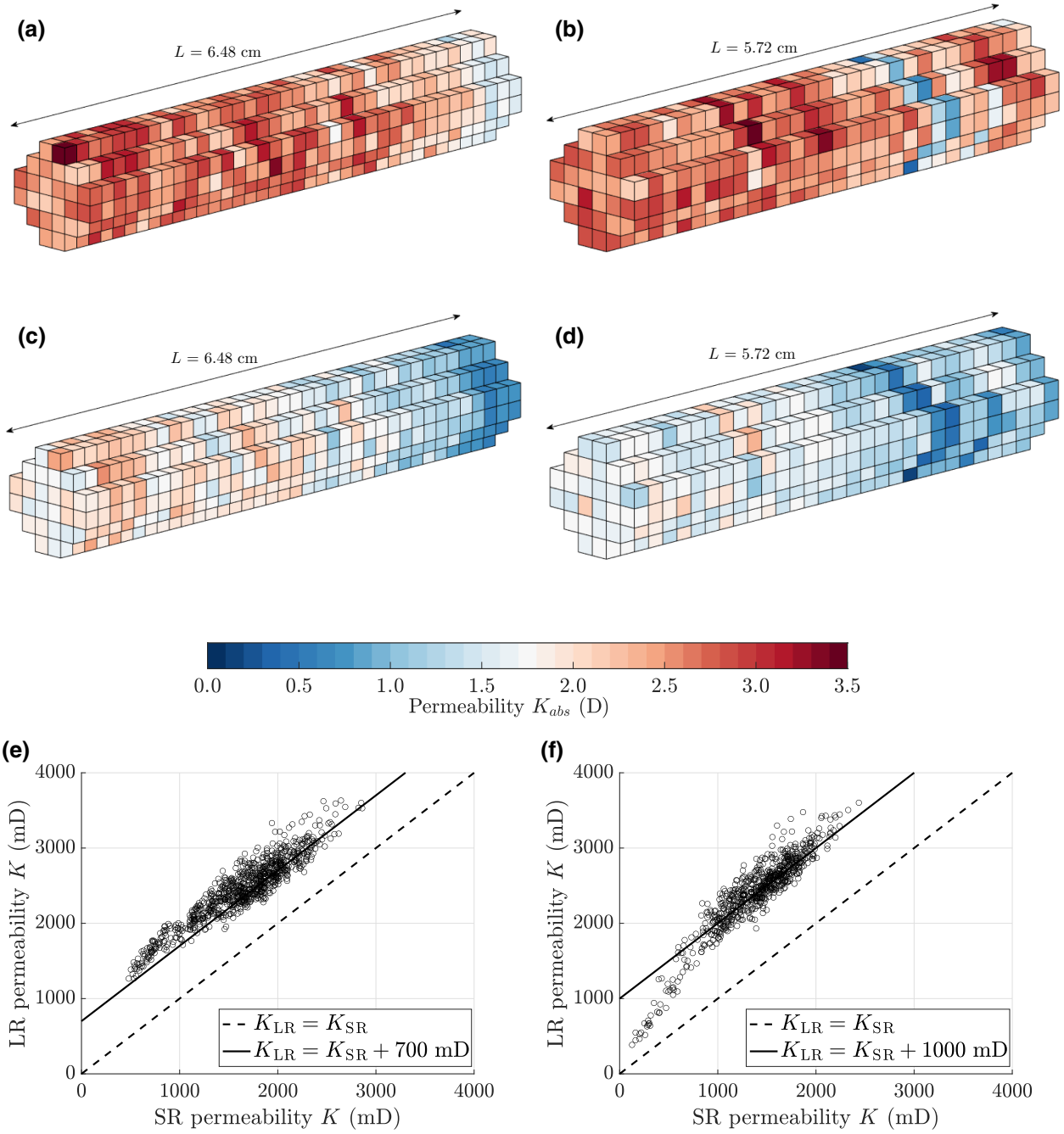

FIG. 8. Continuum-scale permeability results from the PNM using the LR LT and SR LT images. (a),(c) Voxelized permeability for the core-1 LR and SR models, respectively. (b, d) Voxelized permeability for the core-2 LR and SR models, respectively. The permeability scale bar is shown underneath. The HT images are found in Fig. S7 in the Supplemental Material [66]. (e),(f) SR versus LR voxel permeabilities for cores 1 and 2, respectively.

to the mean, in Table I. We see that the SR results generally have higher V_k, indicating that they have captured more of the heterogeneity of the core. The HT segmentations generally result in lower V_k, as the pore space has been more strongly eroded, with higher connectivity, resulting in less permeability variation across the REVs.

In Table I, we see that the HT realizations generally overestimate the permeability for both the LR and SR cases, since the pore space has been eroded and enlarged. This increases local conductivity between pores and the overall core-averaged conductivity and/or permeability. At the lower threshold, the SR-based model has an accurate prediction of the permeability for core 1 (8.1% error); this

threshold is chosen to approximate the macroscopic porosity in the sample that contributes to flow. When combined with the more accurate SR pore-space representation, this threshold gives a good estimate of the connected flow path and hence the permeability. However, for core 2, the SR LT model overpredicts the permeability (85.0% error), although it is more accurate than the other models. For core 2, the 3D permeability map in Fig. 8(d) shows a very-low-permeability band cutting oblique to the flow direction, with permeability $O(100)$ mD. This band is the primary control on the core average permeability (through the harmonic mean), with the rest of the core otherwise quite similar to the more homogeneous core 1 (i.e., approximately 1.5 D). Simulations show that reducing the permeability of cells within the band to 10% of their original values (now ranging from 10 to 50 mD) reduces the average permeability to 793.2 mD, in line with the experimental value (16.5% error). These low values are likely linked to the hematite inclusions in the band, which reduce intergranular porosity and permeability. It is likely that even the HR image of this region (the core 2 subvolume 2 data), at 2-μm resolution, is still not able to fully resolve some small throats that are controlling the resistance to flow. With this, the SR image is also not able to capture the same features and may need a higher-resolution training data set for capturing the very low permeability here. In previous works, models of resolution 2–5 μm have been used to accurately capture permeabilities of > 100 mD [13,19]. However, for smaller permeabilities of $O(10)$mD, [72] have used resolutions < 1 μm, which may be required for the heterogeneous regions here. This highlights the care that must be taken when using real heterogeneous media that could have regions of very reduced permeability in a system of overall quite high average permeability.

When comparing the LR and SR results directly in Figs. 8(e) and 8(f), we see that the LR results are highly correlated with the SR results at high permeability but offset by a constant (approximately +700 mD for core 1, approximately +1000 mD for core 2). At permeabilities < 1 Darcy, the results are less correlated; this suggests that the connectivity in the microstructure is fundamentally different in the segmentations of the tight regions and not as accurately captured by the LR image. At higher permeability, the constant offset suggests that although porosity between the models is very well matched, the LR model is consistently not resolving some small features below a threshold. To achieve the same porosity, some of the larger regions are essentially eroded, resulting in larger conductivities. The permeability difference between LR and SR is near constant, since these features are consistently missing in each LR image that represents a REV for permeability.

We note that further reductions to the segmentation threshold value do not significantly lower the permeability predictions, which can actually inflect and start to increase the permeability past a given low threshold [45]. This is because lowering the threshold contracts the pores and throats, eventually entirely removing some small throats (which were greatly increasing resistance to flow). This results in flow through larger throats with increased permeability. This also helps to explain why the SR models generally have lower permeability predictions than the LR, since smaller throats are actually resolved and can contribute to flow resistance in the network.

Further from the single-phase predictions, we present multiphase-flow predictions in the form of relative permeability and saturation in Fig. 9 for the SR LT model, and tabulated results for the LR and SR LT models in Table II (further results are in the Supplemental Material [66]: Table S1 shows LR and SR HT results and Figs. S10–S12 show the LR LT, LR HT and SR HT model results, respectively). We see that core average relative permeabilities are generally well predicted by the SR LT model along with 3D voxel and slice average saturations along the profile of the core. Overall, the SR LT model represents the most accurate model when considering both saturation and pressure predictions. The core average saturations are predicted to within the experimental repeatability ($\pm 10\%$), apart from $f_o = 1$ in core 1. This is highlighted in Figs. 9(a) and 9(c), whereby the saturations are correlated but raised relative to the experimental results. There are strong capillary-end effects in the model, which are not as prominent in the experiment. The higher-threshold models in Figs. S10–S12 in the Supplemental Material [66] show fewer end effects, due to a lower P_c transition at the outlet and may be more representative of the true experiment. In the models, we use a constant core average capillary pressure at the outlet ($P_c = P_e = 3.7$ kPa) and note that the model is slightly shorter than the full core due to imaging artifacts. The images are missing approximately 5 mm from each end, equivalent to 2.5 grid blocks (the missing regions are visible in the lack of data at $x/L < 0.07, x/L > 0.93$). Without calibration of the outlet P_c [6] or artificial extensions to the model geometry [48], we generally overpredict end effects at high f_o. We choose to have a calibration-free model here, which provides robust results for cases with small end effects ($f_o < 1$) and allows bias-free modeling of the process.

In general, we see that the saturation predictions of the LR and SR models are similar; however, the SR model gives a marginally better representation of saturation heterogeneity in the core, likely due to a slightly more accurate capillary pressure near the percolation threshold. The relatively good performance of both models suggests that saturation heterogeneity is not strongly linked to the functional representation of capillary pressure here but, instead, related to the relative variation in capillary pressure through the core, as shown in Ref. [48]. Even though the LR capillary pressures do not capture the overall shape from $0.2 < S_w < 0.8$ as well as the SR model [see

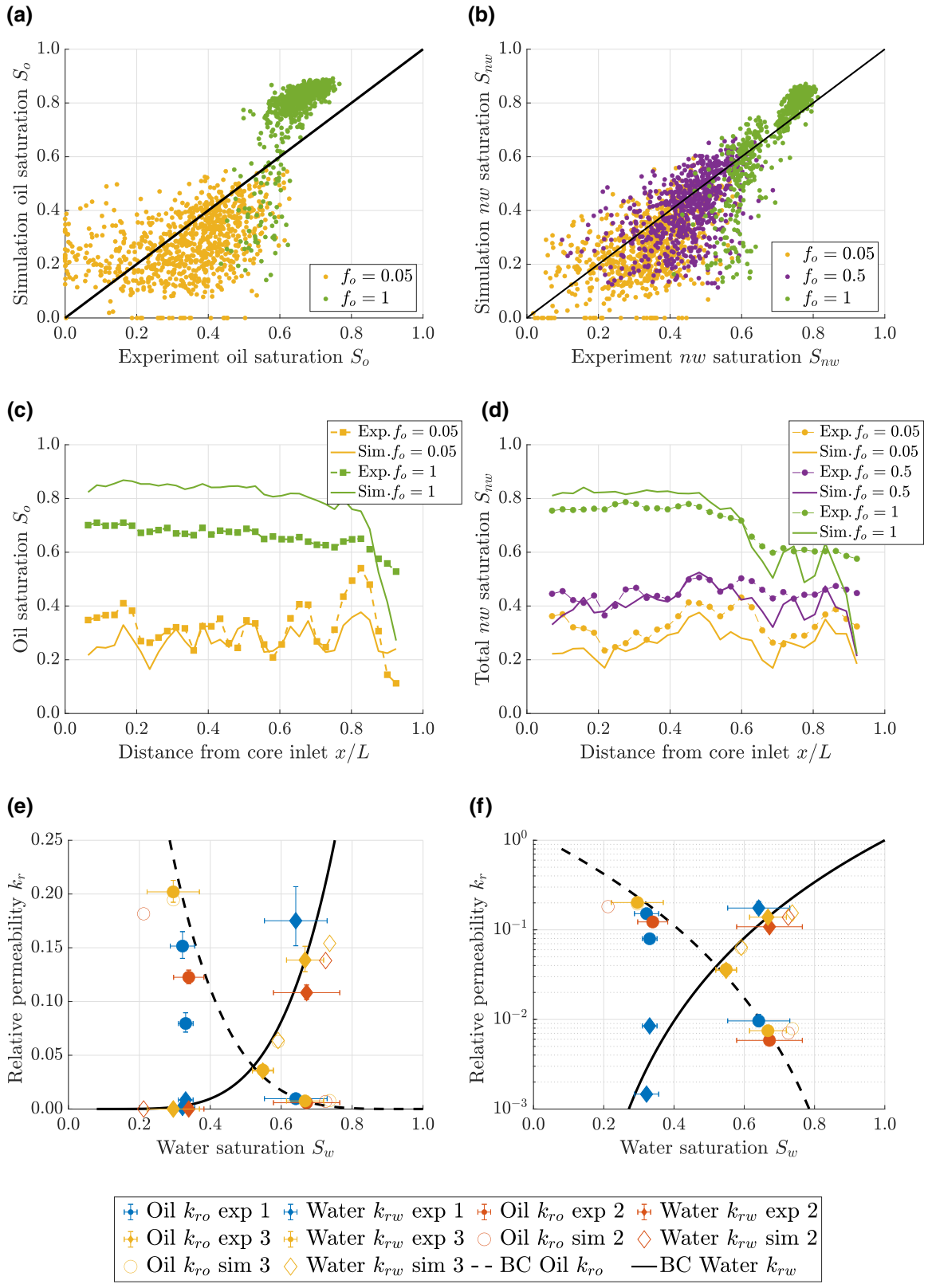

FIG. 9. Whole-core saturations and relative permeabilities for the experiments and simulations. Simulations are shown for the model derived from SR LT images: further realizations can be found in the Supplemental Material [66]. (a),(b) Voxelized saturations for cores 1 and 2, respectively. (c),(d) Slice average saturations for cores 1 and 2, respectively. (e),(f) Linear and logarithmic relative permeability results, respectively. The relative permeability legend is shown underneath the plots: the open symbols are the simulations and the closed symbols are the experiment. Note that here we simulate "exp 2" and "exp 3" from Ref. [6].

TABLE II. Multiphase-flow-simulation results compared to experiments. Results are shown for models derived from the low-threshold (LT) images. Lines showing simulation error (%) are in bold. The high-threshold (HT) results are shown in the Supplemental Material [66].

	Core 1				Core 2					
	LR		SR		LR			SR		
Fractional flow of oil, f_o	0.05	1	0.05	1	0.05	0.5	1	0.05	0.5	1
S_w average experiment	0.672	0.339	0.672	0.339	0.667	0.548	0.296	0.667	0.548	0.296
S_w average simulation	0.726	0.256	0.725	0.212	0.730	0.589	0.299	0.737	0.591	0.296
S_w average error (%)	**8.1**	**−24.6**	**8.0**	**−37.5**	**9.4**	**7.4**	**1.1**	**10.4**	**7.8**	**0.1**
k_{ro} experiment	0.005 84	0.123	0.005 84	0.123	0.007 48	0.0362	0.202	0.007 48	0.0362	0.202
k_{ro} simulation	0.007 84	0.238	0.007 04	0.182	0.007 83	0.0629	0.230	0.007 89	0.0627	0.195
k_{ro} error (%)	**34.2**	**94.4**	**20.6**	**48.2**	**4.6**	**73.6**	**13.8**	**5.4**	**73.0**	**−3.7**
k_{rw} experiment	0.108	0	0.108	0	0.139	0.0353	0	0.139	0.0353	0
k_{rw} simulation	0.162	0	0.138	0	0.160	0.0664	0	0.154	0.0637	0
k_{rw} error (%)	**49.3**	**0**	**27.6**	**0**	**15.7**	**87.9**	**0**	**11.2**	**80.3**	**0**

Figs. S8(c) and (f) and S9(c) and (f) in the Supplemental Material [66]], they still capture the relative variation between regions and hence the saturation heterogeneity in the model. We see that relative permeability heterogeneity [see Figs. S8(a), (b), (d), and (e) and S9(a), (b), (d), and (e) in the Supplemental Material [66]] does not contribute strongly to saturation heterogeneity, as also shown in Ref. [48].

The relative permeability predictions from the SR LT model are more accurate than those of the LR LT model and the other HT models. We are able to capture the relative permeability to within the same order of magnitude (often $< 20\%$ error) across 3 orders of magnitude in range. The nonwetting core average relative permeability [Figs. 9(e) and 9(f)] in each case is equivalent to the average of the individual subvolume relative permeabilities (Figs. S8 and S9 in the Supplemental Material [66]) with some degree of end effect, depending on the fractional flow, with larger impacts at higher f_o. The type of average is likely harmonic, or similar, given the lower bounding of the subvolume relative permeabilities by the core-average results. For the wetting relative permeability, the core average looks to be a simple arithmetic average of the subvolume individual values [see Figs. S8(b) and (e) and S9(b) and (e) in the Supplemental Material [66]]. This is physically intuitive, since the wetting fluid remains connected at all modeled saturations.

Similar to the saturation prediction, the LR-model prediction of relative permeability is worse than that of the SR, but not significantly (see Table II). However, we note that the pressure predictions are significantly worse in the LR model during both single and multiphase flow compared to the SR model. The less accurate pressure prediction does not necessarily translate directly to relative permeability, since relative permeability essentially acts as a ratio between the core-averaged single-phase and multiphase permeability at a given saturation. In the low-capillary-number high-S_w flow regime here, flow is controlled strongly by the largest percolating pathway through the core. The flow is well modeled through this pathway, even at low resolution, with the other regions behaving as single-phase flow conduits. These single-phase flow regions have the same inaccurate pressure contribution as per the absolute permeability calculation and therefore essentially cancel out when considering the relative permeability. For more uniform displacement fronts, at higher capillary number or at lower S_w, it is likely that the SR model will behave significantly better than the LR model, as more of the pore space is utilized and the resolution of smaller throats will become more important. This will also be true in systems with more heterogeneous flow paths and larger ratios between pore body to throat sizes (e.g., carbonate systems).

We see that the relative permeability at $f_o = 0.5$ in the core-2 experiment is not well captured by any model and suggests an epistemic uncertainty. In the models, we only simulate the drainage process but during the $f_o = 0.5$ coinjection, it is likely that both drainage and imbibition displacement mechanisms are occurring. If local trapping is also occurring, this could explain the lower experimental k_r due to an increased resistance to flow. It is also possible that flow intermittency [73] is occurring at this fractional flow due to the increased multiphase competition, which is not represented in the model. Intermittency generally results in more energy dissipation, meaning that relative permeabilities will be lower than in the connected-pathway case.

Overall, we see that the SR models are able to accurately reproduce the experimental behavior of the continuum-scale system and are generally more accurate than the basic LR-derived models. We can capture the key saturation and pressure behavior over a range of conditions during drainage. For the experimental conditions simulated in this paper, the largest improvements compared to the SR model are seen in pressure and absolute-permeability predictions, which have contributions from a wide range of pore body

and throat sizes. We also see improvements in capturing saturation heterogeneity (see the voxel saturation plots) and relative permeability in the SR model but the benefits are not as strong when flow is controlled by large connected pore bodies and throats, which are already well resolved in the LR model. This is a consequence of the resolution chosen and the available experimental data, which constrain the "low-resolution" data. Based on this, further exploration of lower-resolution systems is warranted, perhaps moving between 20-μm and (1–2)-μm resolutions (in multiple steps to aid information transferal) where the underlying full-core images are themselves not able to accurately capture the main percolating pathways.

IV. CONCLUSIONS

In this work, we develop an EDSR neural network to overcome traditional field-of-view and resolution trade-offs in x-ray micro-CT imaging of multiscale porous media. We develop the deep-learning architecture in 3D using paired LR and HR data from optically magnified x-ray CT images across multiple subvolumes. We test the network on unseen LR and HR data from the relatively homogeneous Bentheimer used for training, as well as a more heterogeneous Bentheimer sample with a distinct microstructure; low-permeability bands with significant hematite mineral inclusions. The proposed network architecture works well at alleviating common imaging defects (ring and beam-hardening artifacts) that are common in HR micro-CT images. The 3D EDSR network is able to produce physically realistic SR images from the input LR images, which emulate the true HR images across a variety of image measures (SSIMs and textural analysis) as well as in multiphase-flow simulations using pore-network modeling. We provide a robust validation of the SR pore-scale behavior using images from several segmentation realizations, removing image-processing bias.

We use the trained EDSR network to validate the approach against experimental data from Ref. [6]. We generate approximately 1000 HR REV-scale subvolumes for each whole core from the LR data. With this, we populate a continuum model, at centimeter scale, with petrophysical properties generated from the subvolume pore-network models. The continuum model is used to simulate drainage-immiscible multiphase flow at low capillary number across a range of fractional flows, comparing directly to experiments. We find that the EDSR-generated model is more accurate than the base LR model at predicting experimental behavior in the presence of heterogeneities, especially in flow regimes where a wide distribution of pore sizes are encountered. The models are generally accurate at predicting saturations to within the experimental repeatability and relative permeability across 3 orders of magnitude. We find less improvement in the EDSR model when the main flow paths are already captured by the LR images, with the saturation heterogeneity and the (low-capillary-number) relative permeability largely controlled by the largest pores in the domain.

The demonstrated methodology is fully deterministic and opens up the possibility to image, simulate, and analyze flow in truly multiscale heterogeneous systems that are otherwise intractable. Further from the digital-rock-physics applications in this work, the methodology can be useful generally in materials-science research with multiscale porous systems. In particular, the design and optimization of heterogeneous lithium-ion batteries could be improved with accurate multiscale characterization [74] and for hierarchical phase change systems with nano- and macroporous components [75].

As well as the multiscale aspects considered in this work, the methodology also has the potential to improve time-resolved x-ray CT imaging, by permitting coarser and therefore faster imaging of large systems. When combined with recent deep-learning noise-removal techniques [71], this could significantly speed up acquisition times and allow the imaging of pore-scale dynamic processes over continuum scales in the laboratory.

Further work considering greater differences in resolution between LR and HR data is being considered using a multiscale deep-superresolution network as per Ref. [35]. Here, training data are required at multiple resolutions, with information linked across scales. This could represent a viable tool for increasing scalability further. Alongside this, approaches that do not require paired input data, e.g., those based on GANs [44,76], could be utilized. Initial results from GANs trained on unpaired data suggests that they can achieve similar performance to a CNN trained on paired data [76]. This could open up the possibility of training with decoupled images from data-storage platforms to exploit the wide range of available data already present in the literature. With this, unpaired data at different resolutions with a multiscale network could also be exploited.

The data and codes used in this work, which provide a robust data set to test different deep-learning models, are open access. The original data set from Ref. [6] is hosted on the BGS National Geoscience Data Centre [77] (there is also a subvolume image data set, for easier download, available on the Digital Rocks Portal [78]). The new LR (6-μm resolution), HR (2-μm resolution), and additional VLR (18-μm resolution) subvolume images are hosted on Zenodo [79]. We host the deep-learning code, as well as MATLAB files for processing the images, and generating input files for the PNM and continuum modeling, on Github [80]. Users can download the PNEXTRACT and PNFLOW software from Refs. [81,82]. IMEX is available at cost from the Computer Modelling Group (CMG); however, equivalent results have been obtained for the continuum-modeling approach using the open-source MOOSE package [83],

running the FINCH application [84]. Examples are provided therein for running core-flood simulations and the CMG input files can be readily converted to the MOOSE syntax. We welcome all future developments on this topic.

ACKNOWLEDGMENTS

We are grateful to Dr. Samuel Krevor from Imperial College London for access to the Zeiss micro-CT scanner. We acknowledge the Computer Modelling Group (CMG) for providing access to IMEX. The authors have no conflicts of interests.

[1] H. Moussaoui, J. Laurencin, Y. Gavet, G. Delette, M. Hubert, P. Cloetens, T. Le Bihan, and J. Debayle, Stochastic geometrical modeling of solid oxide cells electrodes validated on 3D reconstructions, Comp. Mater. Sci. **143**, 262 (2018).

[2] P. Fantazzini, R. J. S. Brown, and G. C. Borgia, Bone tissue and porous media: Common features and differences studied by NMR relaxation, Magn. Reson. Imaging **21**, 227 (2003).

[3] R. H. Vernon, *A Practical Guide to Rock Microstructure* (Cambridge University Press, Cambridge, UK, 2018).

[4] P. Ringrose and M. Bentley, *Reservoir Model Design: A Practitioners Guide* (Springer, Dordrecht, 2015).

[5] H. Menke, C. Reynolds, M. Andrew, J. P. Nunes, B. Bijeljic, and M. Blunt, 4D multi-scale imaging of reactive flow in carbonates: Assessing the impact of heterogeneity on dissolution regimes using streamlines at multiple length scales, Chem. Geol. **481**, 27 (2018).

[6] S. J. Jackson, Q. Lin, and S. Krevor, Representative elementary volumes, hysteresis, and heterogeneity in multiphase flow from the pore to continuum scale, Water Resour. Res. **56**, e2019WR026396 (2020).

[7] L. Vásárhelyi, Z. Kónya, Á. Kukovecz, and R. Vajtai, Microcomputed tomography–based characterization of advanced materials: A review, Mater. Today Adv. **8**, 100084 (2020).

[8] Y. Da Wang, M. J. Blunt, R. T. Armstrong, and P. Mostaghimi, Deep learning in pore scale imaging and modeling, Earth-Sci. Rev. **215**, 103555 (2021).

[9] A. Q. Raeini, M. J. Blunt, and B. Bijeljic, Modelling two-phase flow in porous media at the pore scale using the volume-of-fluid method, J. Comput. Phys. **231**, 5653 (2012).

[10] H. Man and X. Jing, Pore network modelling of electrical resistivity and capillary pressure characteristics, Transp. Porous Media **41**, 263 (2000).

[11] P. Mostaghimi, M. Liu, and C. H. Arns, Numerical simulation of reactive transport on micro-CT images, Math. Geosci. **48**, 963 (2016).

[12] H. P. Menke, J. Maes, and S. Geiger, Upscaling the porosity-permeability relationship of a microporous carbonate for Darcy-scale flow with machine learning, Sci. Rep. **11**, 1 (2021).

[13] P. Mostaghimi, M. J. Blunt, and B. Bijeljic, Computations of absolute permeability on micro-CT images, Math. Geosci. **45**, 103 (2012).

[14] V. Cnudde and M. N. Boone, High-resolution x-ray computed tomography in geosciences: A review of the current technology and applications, Earth-Sci. Rev. **123**, 1 (2013).

[15] B. K. Blykers, C. Organista, M. N. Boone, M. Kagias, F. Marone, M. Stampanoni, T. Bultreys, V. Cnudde, and J. Aelterman, Tunable x-ray dark-field imaging for sub-resolution feature size quantification in porous media, Sci. Rep. **11**, 18446 (2021).

[16] D. Łydżba, Homogenisation theories applied to porous media mechanics, J. Theor. Appl. Mech. **36**, 657 (1998).

[17] L. Ruspini, P. Øren, S. Berg, S. Masalmeh, T. Bultreys, C. Taberner, T. Sorop, F. Marcelis, M. Appel, and J. Freeman, *et al.*, Multiscale digital rock analysis for complex rocks, Trans. Porous Media **139**, 301 (2021).

[18] S. Wang, L. C. Ruspini, P.-E. Oeren, S. Van Offenwert, and T. Bultreys, Anchoring multi-scale models to micron-scale imaging of multiphase flow in rocks, Earth Space Sci. Open Arch. ESSOAr (2021).

[19] P. W. S. K. Botha and A. P. Sheppard, Mapping permeability in low-resolution micro-CT images: A multiscale statistical approach, Water Resour. Res. **52**, 4377 (2016).

[20] S. S. Panda, M. S. R. Prasad, and G. Jena, POCS based super-resolution image reconstruction using an adaptive regularization parameter, Int. J. Comput. Sci. Issues **8**, 155 (2011).

[21] W. Shen, L. Fang, X. Chen, and H. Xu, Projection onto convex sets method in space-frequency domain for super resolution, J. Comput. **9**, 1959 (2014).

[22] M. E. Tipping and C. M. Bishop, Bayesian image super-resolution, Adv. Neural Inf. Process. Syst., 1303 (2003).

[23] L. C. Pickup, D. P. Capel, S. J. Roberts, and A. Zisserman, Bayesian methods for image super-resolution, Comput. J. **52**, 101 (2008).

[24] W. T. Freeman, T. R. Jones, and E. C. Pasztor, Example-based super-resolution, IEEE Comput. Graph. Appl. **22**, 56 (2002).

[25] J. Salvador, *Example-Based Super Resolution* (Academic Press, London, UK, 2016).

[26] J. Yang, J. Wright, T. Huang, and Y. Ma, in *2008 IEEE Conference on Computer Vision and Pattern Recognition* (IEEE, 2008), p. 1.

[27] J. Yang, J. Wright, T. S. Huang, and Y. Ma, Image super-resolution via sparse representation, IEEE Trans. Image Process. **19**, 2861 (2010).

[28] Z. Zhu, F. Guo, H. Yu, and C. Chen, Fast single image super-resolution via self-example learning and sparse representation, IEEE Trans. Multimedia **16**, 2178 (2014).

[29] S. C. Park, M. K. Park, and M. G. Kang, Super-resolution image reconstruction: A technical overview, IEEE Signal Process. Mag. **20**, 21 (2003).

[30] R. Timofte, V. De Smet, and L. Van Gool, in *Proceedings of the IEEE International Conference on Computer Vision* (2013), p. 1920.

[31] C. Dong, C. C. Loy, K. He, and X. Tang, in *European Conference on Computer Vision* (Springer, 2014), p. 184.

[32] C. Dong, C. C. Loy, and X. Tang, in *European Conference on Computer Vision* (Springer, 2016), p. 391.

[33] J. Kim, J. K. Lee, and K. M. Lee, in *Proceedings of the IEEE Conference on Computer Vision and Pattern Recognition* (2015), p. 1637.

[34] W. Shi, J. Caballero, F. Huszár, J. Totz, A. P. Aitken, R. Bishop, D. Rueckert, and Z. Wang, in *Proceedings of the IEEE Conference on Computer Vision and Pattern Recognition* (2016), p. 1874.

[35] B. Lim, S. Son, H. Kim, S. Nah, and K. Mu Lee, in *Proceedings of the IEEE Conference on Computer Vision and Pattern Recognition Workshops* (2017), p. 136.

[36] C. Ledig, L. Theis, F. Huszár, J. Caballero, A. Cunningham, A. Acosta, A. Aitken, A. Tejani, J. Totz, and Z. Wang, in *Proceedings of the IEEE Conference on Computer Vision and Pattern Recognition* (2017), p. 4681.

[37] X. Wang, K. Yu, S. Wu, J. Gu, Y. Liu, C. Dong, Y. Qiao, and C. Change Loy, ESRGAN: in *Proceedings of the European Conference on Computer Vision (ECCV)* (2018), p. 0.

[38] A. Bulat, J. Yang, and G. Tzimiropoulos, in *Proceedings of the European Conference on Computer Vision (ECCV)* (2018), p. 185.

[39] Y. Yuan, S. Liu, J. Zhang, Y. Zhang, C. Dong, and L. Lin, in *Proceedings of the IEEE Conference on Computer Vision and Pattern Recognition Workshops* (2018), p. 701.

[40] Y. Wang, Q. Teng, X. He, J. Feng, and T. Zhang, CT-image of rock samples super resolution using 3D convolutional neural network, Comput. Geosci. **133**, 104314 (2019).

[41] Y. D. Wang, R. T. Armstrong, and P. Mostaghimi, Enhancing resolution of digital rock images with super resolution convolutional neural networks, J. Pet. Sci. Eng. **182**, 106261 (2019).

[42] H. Chen, X. He, Q. Teng, R. E. Sheriff, J. Feng, and S. Xiong, Super-resolution of real-world rock microcomputed tomography images using cycle-consistent generative adversarial networks, Phys. Rev. E **101**, 23305 (2020).

[43] Y. D. Wang, R. T. Armstrong, and P. Mostaghimi, Boosting resolution and recovering texture of 2D and 3D micro-CT images with deep learning, Water Resour. Res. **56**, e2019WR026052 (2020).

[44] Y. Niu, Y. D. Wang, P. Mostaghimi, P. Swietojanski, and R. T. Armstrong, An innovative application of generative adversarial networks for physically accurate rock images with an unprecedented field of view, Geophys. Res. Lett. **47**, e2020GL089029 (2020).

[45] N. Janssens, M. Huysmans, and R. Swennen, Computed tomography 3D super-resolution with generative adversarial neural networks: Implications on unsaturated and two-phase fluid flow, Materials **13**, 1397 (2020).

[46] G. Garfi, C. M. John, S. Berg, and S. Krevor, The sensitivity of estimates of multiphase fluid and solid properties of porous rocks to image processing, Transp. Porous Media **131**, 985 (2019).

[47] L. Leu, S. Berg, F. Enzmann, R. T. Armstrong, and M. Kersten, Fast x-ray micro-tomography of multiphase flow in Berea sandstone: A sensitivity study on image processing, Transp. Porous Media **105**, 451 (2014).

[48] C. Zahasky, S. J. Jackson, Q. Lin, and S. Krevor, Pore network model predictions of Darcy-scale multiphase flow heterogeneity validated by experiments, Water Resour. Res. **56**, e2019WR026708 (2020).

[49] K. He, X. Zhang, S. Ren, and J. Sun, in *Proceedings of the IEEE Conference on Computer Vision and Pattern Recognition* (2015), p. 770.

[50] D. P. Kingma and J. Ba, Adam: in *3rd International Conference for Learning Representations (ICLR), San Diego* (2015).

[51] Z. Wang, A. Bovik, H. Sheikh, and E. Simoncelli, Image quality assessment: From error visibility to structural similarity, IEEE Trans. Image Process. **13**, 600 (2004).

[52] A. Buades, B. Coll, and J.-M. Morel, Nonlocal image and movie denoising, Int. J. Comput. Vis. **76**, 123 (2007).

[53] T. Bultreys, Q. Lin, Y. Gao, A. Q. Raeini, A. AlRatrout, B. Bijeljic, and M. J. Blunt, Validation of model predictions of pore-scale fluid distributions during two-phase flow, Phys. Rev. E **97**, 053104 (2018).

[54] A. Q. Raeini, B. Bijeljic, and M. J. Blunt, Generalized network modeling: Network extraction as a coarse-scale discretization of the void space of porous media, Phys. Rev. E **96**, 013312 (2017).

[55] H. Dong and M. J. Blunt, Pore-network extraction from micro-computerized-tomography images, Phys. Rev. E **80**, 036307 (2009).

[56] A. Q. Raeini, B. Bijeljic, and M. J. Blunt, Generalized network modeling of capillary-dominated two-phase flow, Phys. Rev. E **97**, 023308 (2018).

[57] P. H. Valvatne and M. J. Blunt, Predictive pore-scale modeling of two-phase flow in mixed wet media, Water Resour. Res. **40**, W07406 (2004).

[58] A. Q. Raeini, J. Yang, I. Bondino, T. Bultreys, M. J. Blunt, and B. Bijeljic, Validating the generalized pore network model using micro-CT images of two-phase flow, Transp. Porous Media **130**, 405 (2019).

[59] G. Mason and N. R. Morrow, Capillary behavior of a perfectly wetting liquid in irregular triangular tubes, J. Colloid Interface Sci. **141**, 262 (1991).

[60] D. E. Goldsack and R. Franchetto, The viscosity of concentrated electrolyte solutions. I. Concentration dependence at fixed temperature, Can. J. Chem. **55**, 1062 (1977).

[61] P. Linstrom, NIST chemistry webbook, NIST standard reference database 69 (1997).

[62] S. A. Ghafri, G. C. Maitland, and J. P. M. Trusler, Densities of aqueous $MgCl_2$(aq), $CaCl_2$(aq), KI(aq), NaCl(aq), KCl(aq), $AlCl_3$(aq), and (0.964 NaCl + 0.136 KCl)(aq) at temperatures between (283 and 472) k, pressures up to 68.5 MPa, and molalities up to 6 mol/kg, J. Chem. Eng. Data **57**, 1288 (2012).

[63] A. Peksa, K.-A. Wolf, and P. Zitha, Bentheimer sandstone revisited for experimental purposes, Mar. Pet. Geol. **67**, 701 (2015).

[64] S. J. Jackson, S. Agada, C. A. Reynolds, and S. Krevor, Characterizing drainage multiphase flow in heterogeneous sandstones, Water Resour. Res. **54**, 3139 (2018).

[65] S. J. Jackson and S. Krevor, Characterization of hysteretic multiphase flow from the mm to m scale in heterogeneous rocks, E3S Web Conf. **89**, 02001 (2019).

[66] See the Supplemental Material at http://link.aps.org/supplemental/10.1103/PhysRevApplied.17.054046 for extra LR, HR, and SR image comparisons, extended pore-network results, and further continuum-modeling results.

[67] L. C. Bam, J. A. Miller, and M. Becker, A mineral x-ray linear attenuation coefficient tool (MXLAC) to assess mineralogical differentiation for x-ray computed tomography scanning, Minerals **10**, 441 (2020).
[68] C. W. Dubelaar and T. G. Nijland, in *Engineering Geology for Society and Territory—Volume 8*, edited by G. Lollino, D. Giordan, C. Marunteanu, B. Christaras, I. Yoshinori, and C. Margottini (Springer International Publishing, Cham, 2015), p. 557.
[69] A. Lange, A. Kupsch, B. Müller, and M. Hentsschel, in *18th World Conference on Nondestructive Testing, 16–20 April 2012, Durban, South Africa* (2012).
[70] R. Pini, S. Krevor, and S. Benson, Capillary pressure and heterogeneity for the CO_2/water system in sandstone rocks at reservoir conditions, Adv. Water Resour. **38**, 48 (2012).
[71] Y. Niu, Y. Da Wang, P. Mostaghimi, J. E. McClure, J. Yin, and R. T. Armstrong, Geometrical-Based Generative Adversarial Network to Enhance Digital Rock Image Quality, Phys. Rev. Appl. **15**, 064033 (2021).
[72] B. Callow, I. Falcon-Suarez, H. Marin-Moreno, J. M. Bull, and S. Ahmed, Optimal x-ray micro-CT image based methods for porosity and permeability quantification in heterogeneous sandstones, Geophys. J. Int. **223**, 1210 (2020).
[73] C. A. Reynolds, H. Menke, M. Andrew, M. J. Blunt, and S. Krevor, Dynamic fluid connectivity during steady-state multiphase flow in a sandstone, Proc. Natl. Acad. Sci. **114**, 8187 (2017).
[74] X. Lu, A. Bertei, D. P. Finegan, C. Tan, S. R. Daemi, J. S. Weaving, K. B. O'Regan, T. M. M. Heenan, G. Hinds, E. Kendrick, D. J. L. Brett, and P. R. Shearing, 3D microstructure design of lithium-ion battery electrodes assisted by x-ray nano-computed tomography and modelling, Nat. Commun. **11**, 2079 (2020).
[75] Y. Grosu, Y. Zhao, A. Giacomello, S. Meloni, J.-L. Dauvergne, A. Nikulin, E. Palomo, Y. Ding, and A. Faik, Hierarchical macro-nanoporous metals for leakage-free high-thermal conductivity shape-stabilized phase change materials, Appl. Energy **269**, 115088 (2020).
[76] Y. Niu, S. J. Jackson, N. Alqahtani, P. Mostaghimi, and R. T. Armstrong, A comparative study of paired versus unpaired deep learning methods for physically enhancing digital rock image resolution, ArXiv:2112.08644v1.
[77] ID No. 130625 at https://dx.doi.org/10.5285/5f899de8-4085-4370-a45e-e613f27e8f1d.
[78] Project 229, DOI:10.17612/KT0B-SZ28, at https://www.digitalrocksportal.org/projects/229.
[79] DOI: https://doi.org/10.5281/zenodo.5542624, at https://zenodo.org/.
[80] https://github.com/sci-sjj/EDSRmodelling.
[81] https://github.com/ImperialCollegeLondon/pnextract.
[82] https://github.com/ImperialCollegeLondon/pnflow.
[83] https://github.com/idaholab/moose.
[84] https://github.com/cpgr/finch.